SAND98-0995

Image Appraisal for 2D and 3D Electromagnetic Inversion

David L. Alumbaugh and Gregory A. Newman

Sandia National Laboratories

PO Box 5800, MS 0750

Albuquerque, NM 87185

Phone: 505-844-0555

Fax: 505-844-7354

Email:dlalumb@sandia.gov

98-0995

1/11/99

Presented at the 1998 Society of Exploration Geophysicists Annual Meeting

New Orleans, Louisiana. 9/98

See 6,7,18

DISCLAIMER

DISCLAIMER

Portions of this document may be illegible in electronic image products. Images are produced from the best available original document.

Abstract

Linearized methods are presented for appraising image resolution and parameter accuracy in images generated with two and three dimensional non-linear electromagnetic inversion schemes. When direct matrix inversion is employed, the model resolution and posterior model covariance matrices can be directly calculated. A method to examine how the horizontal and vertical resolution varies spatially within the electromagnetic property image is developed by examining the columns of the model resolution matrix. Plotting the square root of the diagonal of the model covariance matrix yields an estimate of how errors in the inversion process such as data noise and incorrect apriori assumptions about the imaged model map into parameter error. This type of image is shown to be useful in analyzing spatial variations in the image sensitivity to the data. A method is analyzed for statistically estimating the model covariance matrix when the conjugate gradient method is employed rather than a direct inversion technique (for example in 3D inversion). A method for calculating individual columns of the model resolution matrix using the conjugate gradient method is also developed. Examples of the image analysis techniques are provided on 2D and 3D synthetic cross well EM data sets, as well as a field data set collected at the Lost Hills Oil Field in Central California.

Introduction

Great advances have been made over the last decade in two and three dimensional electromagnetic imaging. In conjunction with these developments there have been several analyses where linearized approximations (e.g. Torres-Verdin, 1991, Zhou et al.,1993, Spies and Habashy, 1995) or non-linear inversion model studies (e.g. Alumbaugh and Morrison, 1995) have been employed for experimental design. Additional work has also been undertaken to posteriorly appraise 1D electrical and electromagnetic inversion results (e.g. Parker, 1980; Oldenburg, 1983; Dosso and Oldenburg, 1989 and 1991; Sen et al., 1993), that is determine the resolution of , and estimate the error in the inverted the 1D model.

To date little work has been done on 2D and 3D posterior image appraisal for electromagnetic inversion. Thus far the work that has been presented has focused on the DC resistivity problem. Ramirez et al. (1995) analyzed the diagonal of the model resolution matrix (**MRM,** also known as the parameter resolution matrix) as defined in Jackson (1972) and Menke (1984), to analyze the resolution of cross hole DC resistivity surveys. They demonstrate that if the inverse of the diagonal is plotted, large values correspond to poor resolution while smaller values correspond to better resolution. For a non-linear analysis, Oldenburg and Li (1998) analyze the image resolution for surface DC resistvity arrays through a depth of exploration study. Their scheme requires running two successive inversions starting with different background models. Regions that show large changes between the two inversions are poorly resolved, while those that show little change are well resolved.

For the posterior appraisal of 2D and 3D electromagnetic inversion results, we extend the work of Ramirez et al. (1995) to include the analysis of the model covariance matrix (**MCM**) (Menke, 1984; Tarantola, 1987) in addition to the **MRM**. The **MCM** estimates how errors within the inversion process such as data noise and inappropriate apriori assumptions about the model are mapped into parameter error. We also demonstrate how these matrices can be estimated when iterative conjugate gradient methods rather than direct inversion techniques are employed. The use of iterative solving methods becomes important as the size of the inverse problem increases such that it is prohibitive to store the sensitivity matrix.

It must be noted that the measures we are analyzing here are approximations that have been linearized about the final model of an iterative, non-linear inversion process. Thus the accuracy of this type of analysis in terms of resolving the full non-linear nature of the problem is limited. However, as it will be demonstrated using both synthetic and field cross well data sets, these calculations do yield valuable information about image resolution and accuracy.

2.5D Image Appraisal Using Direct Inversion

The inversion scheme employed in this portion of the analysis is a 2.5D version of the scheme outlined in Newman and Alumbaugh (1997). The natural logarithm of the updated model at iteration i+1 is given by

$$\ln(\mathbf{m}^{(i+1)} - \mathbf{l}) = \left[\left(\mathbf{DA}'^{(i)}\right)^T \left(\mathbf{DA}'^{(i)}\right) + \lambda^{(i)}\mathbf{W}^T\mathbf{W}\right]^{-1} \left(\mathbf{DA}'^{(i)}\right)^T \mathbf{D}\delta\mathbf{d}^{(i)} \qquad (1)$$

where

$$\left(\mathbf{DA}'^{(i)}\right)^T \mathbf{D}\delta\mathbf{d}^{(i)} = \left(\mathbf{DA}'^{(i)}\right)^T \mathbf{D}\left(\mathbf{d_m} - \mathbf{d}^{(i)} + \mathbf{A}'^{(i)} \ln(\mathbf{m}^{(i)} - \mathbf{l})\right). \qquad (2)$$

Here **D** is the data weighting matrix (the inverse of the estimated data standard deviations), **W** represents the Laplacian smoothing matrix which stabilizes the inversion process, $\lambda^{(i)}$ is the tradeoff parameter at the ith iteration that weights model smoothness against data fit, $\mathbf{d_m}$ is the measured data, $\mathbf{d}^{(i)}$ the predicted data at the ith iteration, **l** the lower bound on the conductivity, $\mathbf{m}^{(i+1)}$ the updated model, and $\mathbf{m}^{(i)}$ the current model. $\mathbf{A}'^{(i)}$ is the logarithmically parameterized Jacobian or sensitivity matrix computed from the model at the ith iteration, which in component form is given by

$$A'^{(i)}_{jk} = A^{(i)}_{jk}(m^{(i)}_k - l_k) = \frac{\partial d^{(i)}_j}{\partial m^{(i)}_k}(m^{(i)}_k - l_k) \qquad (3)$$

where the *j* subscript refers to jth datum, and the *k* the kth model parameter, and $A^{(i)}_{jk}$ represents the non-logarithmically paramaterized sensitivity matrix. Note, that the natural logarithm of the model parameters is employed to enforce positivity constraints. However, rather than employing the natural logarithm function as a vector operation as implied in Equations (1) and (2), we actually compute the natural logarithm of each element of the vector; it is been written in these equations as a vector operation for notational simplicity. Finally, when performing the natural logarithmic calculations, we assume that the values within the brackets have been normalized such that they are dimensionless.

For more details on the inversion procedure and how different components are calculated, the reader is referred to Newman and Alumbaugh (1997). However, a major difference between this 2.5D scheme and the 3D scheme of Newman and Alumbaugh (1997) is that here an lower/upper (LU) decomposition (Press et al., 1986) is employed to directly compute the inverse matrix; the 3D scheme employs the iterative conjugate gradient method as described below to determine the model update.

To demonstrate the applicability of the various appraisal techniques, we will employ the model shown in Figure 1a which consists of two 2D blocks (0.5 S/m and a 0.25 S/m) embedded in a 0.1 S/m whole space. Note, cross well data were chosen here due to the fact that we had access to good quality field data. However, the methods presented here will work on any type of recording geometry. Synthetic data were generated using the code outlined in Newman and Alumbaugh (1995) for 16 vertical magnetic dipole (VMD) sources in the left well, and 16 receivers in the right. A frequency of 1 KHz was employed, and random noise with a standard deviation equal to 0.5% of the data amplitude were added to each datum. Fourteen iterations were needed to produce the image in Figure 1b. During this process the χ^2 error defined as the mean squared difference between the weighted predicted and measured data was reduced from 5700 to 1, and the tradeoff parameter (λ_i) was reduced from 76,642 to 37.

The Model Resolution Matrix

If we assume that in the linearized limit at iteration i we are very close to reproducing the true model, then by performing a Taylor's Series expansion about the true model $\overline{\mathbf{m}}$ (see Appendix A) we can approximate Equation (2) as

$$\delta\mathbf{d}^{(i)} = \mathbf{d}_{\mathbf{m}} - \mathbf{d}^{(i)} + \mathbf{A}'^{(i)} \ln(\mathbf{m}^{(i)} - \mathbf{l}) \approx \mathbf{A}'^{(i)} \ln(\overline{\mathbf{m}} - \mathbf{l}). \qquad (4)$$

This allows us to rewrite Equation (1) as

$$\ln(\mathbf{m}^{(i+1)} - \mathbf{l}) \approx \mathbf{MRM} \ln(\overline{\mathbf{m}} - \mathbf{l}) \qquad (5)$$

where

$$\mathbf{MRM} = \left[\left(\mathbf{DA}'^{(i)}\right)^T \left(\mathbf{DA}'^{(i)}\right) + \lambda^{(i)} \mathbf{W}^T \mathbf{W}\right]^{-1} \left(\mathbf{DA}'^{(i)}\right)^T \mathbf{DA}'^{(i)} \qquad (6)$$

is the model resolution matrix.

Notice that the **MRM** can be thought of as a filter which when applied to the true model results in the imaged model. Ideally the **MRM** should be an identity matrix which would imply perfect resolution (Menke, 1984). However, because the problem is underdetermined, and because we are smoothing the model through the use of the Laplacian smoothing matrix **W**, we can not resolve each parameter uniquely. Rather each parameter value within the imaging region results from an averaging process, where the averaging occurs over other parameters adjacent to the one of interest. The function describing this averaging process is defined by Backus and Gilbert (1968,1970) as the resolution kernel or the 'Point Spread Function' (PSF). The greater the area (or volume) over which this averaging occurs, the poorer the resulting resolution of an individual

parameter, and the less the **MRM** resembles **I,** the identity matrix. In addition, as the **MRM** continues to deviate from the identity matrix, the diagonal elements continue to decrease in magnitude. Thus by plotting the elements of the main diagonal in the same format as the model vector, we can discern the relative resolution from one point to another within the image domain.

In Figure 2 we have plotted $1/(4\pi*\mathrm{MRM}_{jj})$ which Ramirez et al. (1995) termed the 'Resolution Radius'. Because we are taking the inverse of the diagonal, greater values infer poorer resolution (greater spatial averaging), while smaller values infer better resolution. Notice that we have better resolution near the wells than in the center of the image, and poorer resolution at the top and bottom of the image. This agrees with what we would expect from a cross well imaging experiment. Also notice that we have better resolution within the conductive zones than outside them.

We believe that even more information can be provided from the **MRM** if we return to the idea of it behaving as an averaging or low pass filter. The PSF defined by Backus and Gilbert (1968,1970) can be estimated at any point in the image plane by replacing the $\ln(\overline{\mathbf{m}}\text{-}\mathbf{l})$ in Equation (5) with a Kronecker Delta function centered at the point of interest, i.e.;

$$\mathbf{r}_j = \left[\left(\mathbf{DA}'^{(i)}\right)^T\left(\mathbf{DA}'^{(i)}\right) + \lambda^{(i)}\mathbf{W}^T\mathbf{W}\right]^{-1}\left(\mathbf{DA}'^{(i)}\right)^T\left(\mathbf{DA}'^{(i)}\right)\boldsymbol{\delta}_j = \mathbf{MRM}\cdot\boldsymbol{\delta}_j, \quad (7)$$

where $\boldsymbol{\delta}_j$ is the Kronecker Delta vector with unity in the jth position and zeros everywhere else. Examining this operation we find that it recovers the jth column of the

MRM. Thus we can analyze the Backus-Gilbert spread function for any point in the image plane by plotting the appropriate column of the **MRM**.

Examples of the PSF for four different locations within the model domain are given in Figure 3. Notice that the spatial averaging, especially in the horizontal direction, is greater towards the top of the imaging region than in the middle. Also note that better resolution results near the wells than in the center of the imaging region.

It is obvious that plotting and analyzing the PSF for every location within the model domain would be laborious. An alternative to plotting each and every PSF is to plot some function that yields information on how the width of these averaging functions varies spatially in the horizontal and vertical directions. Here we will employ the 50% spread width, which is defined as the full width of the PSF in either the horizontal or vertical direction at those points where the amplitude is 50% of its maximum value. In the plots in Figure 3, this would correspond to the distance between those points where the normalized value is equal to 0.5.

Figure 4 shows the results of performing this operation at every point within the image domain. The first thing that stands out over the analysis provided by Figure 2 but that was apparent in Figure 3 is that the spread values are greater in the horizontal direction than in the vertical, i.e., there is more averaging occurring horizontally then vertically. This agrees with the results of Zhou et al (1993) and Alumbaugh and Morrison (1995) who demonstrated that the vertical resolution is better than that of the horizontal resolution for cross well EM data. An additional interesting note is that the vertical spread appears to be independent of the conductivity structure, while the horizontal

spread is smaller in those areas associated with greater conductivity. This correlates with the wave number domain analysis of Zhou et al. (1993) who showed for the cross well EM configuration that the vertical resolution is dependent only on the source-receiver spatial sampling interval, while the horizontal resolution depends on the conductivity as well as this sampling interval.

The Posterior Model Covariance Matrix

A second tool that we can employ for image appraisal is the model covariance matrix (Menke, 1984; Tarantola, 1987, Meju, 1994). The main diagonal of this matrix estimates how data noise, and errors in the apriori assumptions about the model, are mapped into uncertainty in the parameter estimates. In our case the model errors revolve around the assumption that that the model varies smoothly from one point to another through the use of **W**. The off diagonals of the **MCM** detail how different parameters within the imaging region are correlated to one another. Because this is a linearized operation about the final model in a nonlinear process, we are essentially determining the range of models that exist about our final result with the requirement that they fit the data to the desired error level. As shown in Appendix B, for the non-linear inverse formulation implemented here the **MCM** can be derived via a comparison to the Maximum Likelyhood Method given in Tarantola (1987) to be

$$\mathbf{MCM} = \left[\left(\mathbf{DA}'^{(i)} \right)^T \left(\mathbf{DA}'^{(i)} \right) + \lambda^{(i)} \mathbf{W}^T \mathbf{W} \right]^{-1}. \qquad (8)$$

Note, due to the logarithmic parameterization (Newman and Alumbaugh, 1997), the **MCM** in this form is dimensionless. To correct for this and display the covariance estimates in the units of $(S/m)^2$ we must multiply each element of **MCM** by the appropriate model parameters, i.e.,

$$MCM'_{jk} = (m_j - l_j)(m_j - l_j)MCM_{jk}. \quad (9)$$

However, as it will be shown later, it may not be necessary to perform this operation.

The most common method of analyzing the **MCM** is to plot the square root of the diagonal component, or variance, which yields an estimate of the standard deviation of each parameter . Figure 5a shows the estimated standard deviation for the test model given by the corrected **MCM** (Equation 9). Notice that the largest standard deviations occur within the conductive zones. Because the induction method is more sensitive to conductors than resistors, one would think that these regions would contain low values of uncertainty. In addition we would expect the greatest errors to be present at the top and bottom of the image domain where there is very little sensitivity to the data.

We have found that we can overcome these apparent misconceptions somewhat by normalizing the standard deviations (Figure 5a) by the imaged conductivities themselves (Figure 1b) and displaying the results in terms of a percentage of the parameter estimates. Note that this is equivalent to skipping equation 9 and simply taking the square root of the **MCM** given by Equation 8. Figure 5b shows that this operation produces an uncertainty image that better agrees with what we would expect, that is the largest error

occurs in those regions of low sensitivity of the model to the data, and smaller errors are present within the conductors and next to the boreholes.

One can also plot the columns of the MCM to determine how parameters at different locations within the imaging region are correlated to one another. However, we have found these cross correlation plots offer less insight into the appraisal process than the other methods discussed here, and thus we have chosen not to include any of this type of analysis.

2.5D and 3D Image Appraisal using the Conjugate Gradient Method

As the size of the inversion problem grows, it becomes computationally prohibitive to form and invert the $\left(\mathbf{DA}'^{(i)}\right)^T\left(\mathbf{DA}'^{(i)}\right)+\lambda^{(i)}\mathbf{W}^T\mathbf{W}$ matrix due to computer memory limitations. In these cases it is often better to employ an iterative method such as the Conjugate Gradient (CG) scheme developed by Hestenes and Stiefel (1952). This method iteratively determines the solution ($\mathbf{x}$) to the linear system of equations given by $\mathbf{Kx=s}$ without inverting $\mathbf{K}$. Assuming $\mathbf{K}$ is an n by n matrix and also that exact arithmetic is employed, the method is guaranteed to converge to the correct solution within n iterations as long as $\mathbf{K}$ is symmetric and positive definite. An additional benefit to using the CG approach is that it is easily parallellizeable to run on massively parallel computer architectures, whereas many matrix inversion techniques are not. This is essential as the 3D EM inversion problem is often computationally too demanding to run on normal serial platforms (Newman and Alumbaugh, 1997).

To solve our problem with this technique, we rearrange Equation 1 such that it reads

$$\left[\left(\mathbf{DA}'^{(i)}\right)^T\left(\mathbf{DA}'^{(i)}\right)+\lambda^{(i)}\mathbf{W}^T\mathbf{W}\right]\ \ln(\mathbf{m}^{(i+1)}-\mathbf{l})=\left(\mathbf{DA}'^{(i)}\right)^T\mathbf{D}\delta\mathbf{d}^{(i)}. \qquad (10)$$

We now use the CG method to solve for $\ln(\mathbf{m}^{(i+1)}-\mathbf{l})$. Mackie and Madden (1993) and Newman and Alumbaugh (1997) have shown that when this method is employed for solving the 3D magnetotelluric and controlled source EM inversion problems, respectively, the $\mathbf{A}'^{(i)}$ matrix, and more importantly, the $\mathbf{A}'^{(i)T}\mathbf{A}'^{(i)}$ matrix never needs to be explicitly formed, thus saving computer memory. However, because we don't explicitly calculate the inverse of $\left(\mathbf{DA}'^{(i)}\right)^T\left(\mathbf{DA}'^{(i)}\right)+\lambda^{(i)}\mathbf{W}^T\mathbf{W}$, we can't explicitly form the **MRM** or the **MCM**. Therefore we need to apply a different approach to acquire the information present in these posterior calculations.

It must be mentioned that one approach we could use to estimate both the **MRM** and the **MCM** is to approximate a singular value decomposition of the system via the Lanczos method (Lanczos, 1950), which is related to the CG method. Scales (1989), Zang and McMechan (1995), Minkoff (1996) and Vasco et al. (1998) all use this technique for appraising seismic inversion results. However, a problem with this technique is that the estimates of the eigenvalue/ eigenvector pairs are often corrupted by numerical round off errors causing a loss of orthogonality in the Lanczos vectors. Although this problem can be remedied by partial reorthogonalization schemes (Vasco et al., 1998), this adds additional computational complexity to the problem as it is often difficult to determine when this is needed. Because of this added complexity, and for the sake of consistency,

we have chosen to employ methods to appraise the inversion results that use the slower Conjugate Gradient scheme directly.

To demonstrate the use of the CG approaches analyzed here, in addition to the 2D model given in Figure 1a we will employ a synthetic crosswell data set calculated for the five well model shown in Figure 6a which was originally published in Alumbaugh and Newman (1997). The 3D image produced by the synthetic data is shown in Figure 6b. Note the conductive sediments overlying resistive basement, and the very conductive 'blob' near the center well at 30m depth which represents an injected salt water plume. Imaging the latter was the main objective of this exercise. The image employed 25 VMD source positions in the center well using a 2.5 m source separation, and 11 receivers in each receiver well with a receiver spacing of 5 m. More specifics of the inversion pertaining to this image can be found in Alumbaugh and Newman (1997).

CG Determination of the Model Resolution Matrix

Because we can not invert the appropriate matrix using the CG method , we can not calculate the full **MRM**. However, we can form individual columns of it to examine the PSF at selected points within the image region using the following technique. Rearranging Equation 7 such that the matrix of interest is moved to the left hand side we obtain

$$\left[\left(\mathbf{DA}'^{(i)}\right)^T\left(\mathbf{DA}'^{(i)}\right)+\lambda^{(i)}\mathbf{W}^T\mathbf{W}\right]\mathbf{r}_j=\left(\mathbf{DA}'^{(i)}\right)^T\left(\mathbf{DA}'^{(i)}\right)\boldsymbol{\delta}_j=\left[\left(\mathbf{DA}'^{(i)}\right)^T\left(\mathbf{DA}'^{(i)}\right)\right]_j \quad (11)$$

where $\left[\left(\mathbf{DA}'^{(i)}\right)^T\left(\mathbf{DA}'^{(i)}\right)\right]_j$ represents the jth column of the $\left(\mathbf{DA}'^{(i)}\right)^T\left(\mathbf{DA}'^{(i)}{}_i\right)$ matrix, and now serves as the source vector for the CG routine. By solving this for several different positions (different j's) throughout the 2D or 3D imaging region, the spatial variation in the model resolution can be deduced.

In Figure 7 we have plotted two different views of the point spread function for a point within the Richmond image that was arbitrarily chosen to be x=-3m, y=-3m, z=29m. The upper portion of the figure shows isosurfaces of the PSF at values of ± 30% of the maximum, while the bottom shows the isosurface that exists at +60% of the maximum. A translucent horizontal plane has also been included at z=29m to visually enhance the spatial variation of the function. Notice 1) the large region over which averaging is occurring in order to produce a parameter value at the point of interest, and 2) the large negative side lobe that exists.

In Figure 8 we have taken the analysis one step further by calculating the PSF at 36 points within the z=29m depth plane. A depth slice at z=29m from the image in Figure 6b is included in Figure 8a. Note; the image has been plotted in linear scale rather than logarithmic, and the white dots designate the location of the five wells. The 50% spread width calculated for the 36 PSFs are plotted in Figure 8b for the x direction, Figure 8c for the y direction, and Figure 8d for the z direction. These images have been constructed by determining the appropriate widths at the location of each PSF (designated by the black dots in Figures 8b through 8d) and then interpolating using a Kriging routine. Although this interpolation procedure may not yield the exact value at each point, it does yield a

general sense of how the resolution varies spatially. The primary conclusion that can be made via this analysis is that the resolution is better near the wells and in the regions immediately between the center and outer wells, and poorer in those regions between the outer well pairs. This poor resolution is due to the fact that there were no data calculated with both the source and receiver positioned in adjacent outer wells. Also notice that as expected from our previous results, the vertical resolution is better than that of the horizontal. However, this is only true in those areas immediately between the center and outer wells; the vertical resolution is as poor as the horizontal in those areas along the edges of the imaging region.

It must be mentioned why only 36 PSFs were calculated within a single plane. The first concern is the amount of time it took to compute each column of the **MRM**. Due to memory limitations we are not storing the Jacobian matrix in the 3D inversion scheme, and thus it is essentially recomputed at every iteration within the CG algorithm. Therefore if we run the CG routine for 60 iterations to ensure solution convergence and accuracy, this corresponds to recomputing the Jacobian 60 times for each PSF that we are interested in. This is a great amount of computational effort, even on a massively parallel platform. A second reason for only computing 36 PSFs is that the algorithm was constructed such that each column of the **MRM** is computed and then written to disk. The various widths of each PSF are then determined in a post processing stage after all the files have been moved to an appropriate computer. Manipulating this large amount of data turns out to be a rather time and memory intensive process, and for these reasons, only 36 PSFs were computed. A possibly more efficient manner to construct the

algorithm would be to employ fewer iterations within the CG routine to save time, and then compute the widths of each PSF within the inversion scheme such that the amount of data written to disk is rather small.

CG Determination of the Posterior Model Covariance Matrix

To calculate the **MCM** when employing the CG technique, we employ the Monte Carlo scheme proposed by Matarese (1993) for analyzing seismic travel time tomography. As shown in Appendix B, this method was developed by comparing regularized inversion to the Maximum Likelihood formulation of Tarantola (1987). We first linearize about the final model produced by the iterative non-linear inversion scheme, and then construct L new source vectors $\left(\mathbf{DA}'^{(i)}\right)^T \mathbf{D}\delta\mathbf{d}_l^{(i)}$ by rewriting Equation (2) as

$$\left(\mathbf{DA}'^{(i)}\right)^T \mathbf{D}\delta\mathbf{d}_l^{(i)} = \left(\mathbf{DA}'^{(i)}\right)^T \mathbf{D}\left((\mathbf{d_m} + \boldsymbol{\varepsilon}_l) - \mathbf{d}^{(i)} + \mathbf{A}'^{(i)} \ln(\mathbf{m}^{(i)} - \mathbf{l})\right) + \lambda^{(i)}\mathbf{W}^T\mathbf{h}_l. \quad (12)$$

Here $\boldsymbol{\varepsilon}_l$ is a random number vector of a variance equal to that of the estimated data noise, and $\mathbf{h}_l$ is a similar vector with a variance equal to $1/\lambda_i$ (the meaning of this is discussed more fully in Appendix B). The last iteration of the inversion is then repeated L times using the final image as the starting point, and the covariance matrix calculated as

$$\mathbf{MCM}' = \frac{1}{L}\sum_{l=1}^{L}(\mathbf{m}_l - \mathbf{m}^{(i+1)})(\mathbf{m}_l - \mathbf{m}^{(i+1)})^T. \quad (13)$$

To demonstrate the validity of this technique, and its possible shortcomings, we have calculated **MCM'** for our initial model image in Figure 1b using two different values of L. As shown by comparing Figure 9a to Figure 5b, L=25 is not enough to provide a useful

estimate of the main diagonal of the **MCM**. However, for L =400 (Figure 9b) the estimated **MCM** compares favorably to that calculated using the analytic technique. However the image still appears to be somewhat 'noisy'. Increasing the number of iterations beyond 400 did not appear to decrease this noisy appearance, and thus one draw back of the method is that we won't be able to recover the exact **MCM**. However, we believe that this result is still of high enough quality to provide useful information.

To demonstrate the real benefit of this process, we again turn to the 3D simulation. In Figure 10 we have plotted the estimated normalized standard deviations in two different formats. In Figure 10a we have plotted the results in a format similar to Figure 6, while in Figure 10b we have plotted the entire image volume with all values greater than 2% of the parameter values made invisible. Inherently, regions of low standard deviation imply a greater sensitivity of the model to the data. Thus these plots yield very valuable information on regions that are well constrained versus those regions that are poorly constrained. Notice 1) the regions of highest sensitivity are those regions immediately between the center and the four outer wells (these correlate with the region of maximum resolution in Figure 8) and 2) the sensitivity decreases within the resistive basement. This agrees with the findings in Alumbaugh and Newman (1997) who showed that there was very little sensitivity to features within the basement for this particular model.

Analysis of a Cross Well Data Set

To demonstrate the use of the various appraisal methods on real data, we have applied the techniques to a cross well data set collected between two wells in the Lost

Hills Oilfield in the Central Valley of California. The data were collected in 1997 for Bakersfield Energy Resources by Dr. Michael Wilt of ElectroMagnetic Instruments (EMI), Inc. using a system built by EMI for Schlumberger-Doll Research. The purpose of this survey was to provide a baseline before a water flood began such that the position of the flood could be monitored over time. A VMD source operating at 1KHz was employed in one well and the vertical magnetic fields measured in a second well located approximately 86m away from the first (note: both wells were cased with fiberglass rather than steel). As shown by the conductivity well logs in Figure 11, the geology consists of gently dipping (7^{o}) interbedded oil sands and shales. The data standard deviation was assumed to be 3% of the data amplitude, and fifteen iterations were needed to produce the image in Figure 11. During this process the χ^2 error was reduced from 30 to 1, and the trade-off parameter (λ_i) was reduced from 1 688 898 to 80. It must be noted that to get a reasonable image, the smoothing in the horizontal direction was four times greater than that in the vertical.

The first thing to point out in Figure 11 is that we have reconstructed the general geology. The position of the low conductivity sand is imaged across the interwell region, and corresponds very well with the well logs. Also notice that the routine is trying to image more conductive regions that fall above and below the transmitter-receiver intervals. Finally, the scheme is attempting to image the slightly less conductive zone that occurs between 800 and 820m depth. However, it is unable to extend this zone all the way across between the wells, and thus we see low conductivity features appearing only immediately adjacent to the two wells.

Questions we might hope the appraisal process to answer include why we can not resolve the resistive zone between 800m and 820m depth as extending all the way across between the two wells, and why we can not resolve any of the finer structures that appear in the well logs? To determine the answers we turn to the **MRM**. In Figure 12 we have plotted the 50% widths as calculated on a point by point basis throughout the imaging region. Notice that as expected the vertical resolution is much better than the horizontal. Also notice that the horizontal resolution is poorer within the resistive layer than out side of it. More importantly with regards to our question, notice that the vertical 50% spread near the center of the image is 4 times greater than that near the wells which helps to explain why the resistive zone between 800 and 820m is not shown to extend all the way across the image plane. That is, the greater amount of spatial averaging at the center of the image is 'smearing through' the resistive layer. As an aside, notice that the vertical spread width near the receiver well increases with increasing receiver separation in those regions where the receiver sampling interval is irregular.

A second question we may ask is whether or not the conductive feature at the bottom of the imaging region is real, or if it is an artifact caused by incomplete data coverage in this region? In Figure 13 we have plotted both the unnormalized and normalized standard deviations as determined from the **MCM**. Notice that at the bottom of the figure we have rather large standard deviations indicating a lack of sensitivity of the model to the data within this region. Thus the conductor that appears extending upward from below the interwell imaging regions is probably an artifact caused by a lack of data in this region.

Discussion and Conclusions

In this paper we have analyzed the use of various linearized functionals for posterior image appraisal and analysis for 2D and 3D non-linear electromagnetic inversion. In addition to analytical forms that involve the inverse of a matrix, we have illustrated methods to derive at least certain portions of these functions when iterative Conjugate Gradient techniques are employed when direct matrix inversion is not available. In addition, although we have focused on the crosswell EM problem here, that has only been as a matter of convenience; the methods proposed here could be applied to linearized inversion of any type of EM or other data set. Currently we are looking to apply these techniques to magnetotelluric data as well as cross well GPR travel time data.

One question still unanswered is how reliable these linearized approaches are when analyzing the nonlinear problem. For example the standard deviations in Figure 10 range between 0.5% and 4%, while in Figure 13b they are 2% to 3%. We believe that these estimates are rather small in magnitude given the complexity of the full non-linear 2D and 3D inversion process. Furthermore we believe that these relatively small values are due to the fact that we are linearizing about the final model rather than determining the **MCM** through a non-linear process. It is conceivable that re-running the full nonlinear inversion L times with different data and smoothing vectors may yield very different results than those achieved by linearizing about the final model of the iterative inversion process. Nevertheless, these linear results appear quite reasonable and thus the linearized

approximations are yielding valuable information about the accuracy and resolution provided by the image, and the non-uniqueness of the inversion problem.

Acknowledgments

This work was performed at Sandia National Laboratories with funding provided by the U.S. Department of Energy's Office of Basic Energy Sciences, Division of Engineering and Geoscience. Sandia is a multiprogram laboratory operated by Sandia Corporation, a Lockheed Martin Company, for the United States Department of Energy under Contract DE-AC04-94AL85000. The authors would like to thanks Dr. Michael Wilt of ElectroMagnetic Instruments, Inc. for providing the Lost Hills cross well data set.

References

Alumbaugh, D.L., and Morrison, H.F., 1995, Theoretical and practical considerations for crosswell electromagnetic tomography assuming a cylindrical geometry; Geophysics, **60**, 846-870.

Alumbaugh, D.L. and Newman, G.A., 1997,Three-dimensional massively parallel inversion - II analysis of a crosswell electromagnetic experiment: Geophys. J. Int., **128**,355-363.

Backus, G. E., and Gilbert, J. F., 1968, The resolving power of gross Earth data; Geophys. J. Roy. Astron. Soc., **16**, 169-205.

Backus, G. E., and Gilbert, J. F., 1970, Uniqueness in the inversion of inaccurate gross earth data; Phil. Trans. R. Soc. Lond., A,**266**, 123-192.

Dosso, S. E., and Oldenburg, D. W., 1989, Linear and non-linear appraisal using extremal models of bounded variation; Geophys. J. Int., **99**, 483-495.

Dosso, S. E., and Oldenburg, D. W., 1991, Magnetotelluric appraisal using simulated annealing; Geophys. J. Int., **106**, 379-385.

Hestenes, M.R., and Stiefel, E., 1952, Methods of conjugate gradients for solving linear systems; J. Res. Nat. Bur. Standards, **49**, 409-435.

Jackson, D., 1972, Interpretation of inaccurate, insufficient, and inconsistent data; Geophys. J. Roy. Astron. Soc., **28**, 97-109.

Lanczos, C., 1950, An iterative method for the solution of the eigenvalue problem of linear differential and integral operators: J. Res. Nat. bur. Stand., **45**, 255-282.

Mackie, R.L., and Madden, T.R., 1993, Three-dimensional magnetotelluric inversion using conjugate gradients; Geophys. J. Int., **115**, 215-229.

Matarese, J.R., 1993, Nonlinear travel time tomography: PhD thesis, Mass. Inst. Tech.

Menke, W., 1984, Geophysical Data Analysis: Discrete Inverse Theory; Academic Press, Inc., Orlando, FL.

Meju, M.A., 1994, Geophysical Data Analysis: Understanding Inverse Problem and Theory; Society of Exploration Geophysicists.

Minkoff, S. E., 1996, A computationally feasible approximate resolution matrix for seismic inverse problems: Geophys. J. Int., **126**, 345-359.

Newman, G.A., and Alumbaugh, D.L., 1997, Three-dimensional massively parallel inversion - I. Theory; Geophys. J. Int., **128**, 345-354.

Newman, G.A., and Alumbaugh, D.L., 1995, Frequency domain modeling of airborne electromagnetic responses using staggered finite differences; Geophy. Pros., **43**, 1021-1042.

Oldenburg, D. W., 1983, Funnel functions in linear and non-linear appraisal, J. Geophys. Res., B9, **88**, 7387-7398.

Oldenberg, D.W., and Li, Y., 1998, Estimating depth of investigation in DC resistivity and IP surveys, Geophysics, In Press.

Parker, R. L., 1980, The inverse problem of electromagnetic induction : existence and construction of solutions based on incomplete data; J. Geophys. Res., **85**, 4421-4428.

Press, W. H., Flannery, B. P., Teukolsky, S. A., and Vetterling, W. T., 1986, Numerical Recipes: The Art of Scientific Computing; Cambridge University Press, Cambridge, England.

Ramirez, A.L., Daily, W.D., and Newmark, R.L., 1995, Electrical resistance tomography for steam injection monitoring and controll; J. of Env. and Eng. Geophys., **0**, 39-52.

Scales, J. A., 1989, On the use of conjugate gradient to calculate the eigenvalues and singular values of large, sparse matrices: Geophys. J., **97**, 179-183.

Sen, M. K., Bhattacharya, B. B., and Stoffa, P. L., 1993, Nonlinear inversion of resistivity sounding data; Geophysics, **58**, 496-507.

Spies, B.R., and Habashy, T.M., 1995, Sensitivity analysis of crosswell electromagnetics; Geophysics, **60**, 834-845.

Tarantola, A., and Vallete, B., 1982. Generalized nonlinear inverse problems solved using the least squares criterion; Rev. of Geophys. and Space Phys., **20**, 219-232.

Tarantola, A., 1987, Inverse Problem Theory, Elsevier.

Torres Verdin, C., 1991, Continuous Profiling of Magnetotelluric Fields, PhD thesis, University of California at Berkeley.

Vasco, D. W., Peterson, J. E. Jr., and Majer, E. L., 1998, Resolving seismic anisotropy; sparse matrix methods for geophysical inverse problems : Geophysics, **63**, 970-983.

Zhang, J., and McMechan, G. A., 1995, Estimation of resolution and covariance for large matrix inversions: Geophys. J. Int., **121**, 409-426.

Zhou, Q., Becker, A., and Morrison, H.F., 1993, Audio-frequency electromagnetic tomography in 2-D; Geophysics, **58**, 482-495.

Appendix A : Derivation of the Model Resolution Matrix

We start by rewriting the $\mathbf{d_m} - \mathbf{d}^{(i)}$ term in equation (2) as

$$\mathbf{d_m} - \mathbf{d}^{(i)} = \mathbf{A}'^{(i)}\,\delta\mathbf{m}^{(i)} \tag{A1}$$

where $\delta\mathbf{m}^{(i)}$ is the model update at the ith iteration. We now linearize about the current model ($\mathbf{m}^{(i)}$) and make the approximation that $\mathbf{m}^{(i+1)}$ is linearly close to the true model, $\overline{\mathbf{m}}$, i.e.,

$$\delta\mathbf{m}^{(i)} \approx \overline{\mathbf{m}} - \mathbf{m}^{(i)}. \tag{A2}$$

We can now use the following equations given in Newman and Alumbaugh (1997),

$$\delta\mathbf{m}^{(i)} \approx (\mathbf{m}^{(i)} - \mathbf{l})\delta\ln(\overline{\mathbf{m}} - \mathbf{l}) \tag{A3}$$

and

$$\delta\ln(\overline{\mathbf{m}} - \mathbf{l}) = \ln(\overline{\mathbf{m}} - \mathbf{l}) - \ln(\mathbf{m}^{(i)} - \mathbf{l}), \tag{A4}$$

to rewrite the above expression as

$$\delta\mathbf{m}^{(i)} \approx (\mathbf{m}^{(i)} - \mathbf{l})\left[\ln(\overline{\mathbf{m}} - \mathbf{l}) - \ln(\mathbf{m}^{(i)} - \mathbf{l})\right]. \tag{A5}$$

We now substitute this expression and equation (A1) into part of equation 2 to yield

$$\delta\mathbf{d}^{(i)} \approx \mathbf{A}'^{(i)}(\mathbf{m}^{(i)} - \mathbf{l})\left[\ln(\overline{\mathbf{m}} - \mathbf{l}) - \ln(\mathbf{m}^{(i)} - \mathbf{l})\right] + \mathbf{A}'^{(i)}\ln(\mathbf{m}^{(i)} - \mathbf{l}) \approx \mathbf{A}'^{(i)}\ln(\overline{\mathbf{m}} - \mathbf{l}). \tag{A6}$$

It is easy to see that when this is substituted into Equation (1), the expression for the model resolution matrix given by Equations (5) and (6) results. (Note; this form agrees with Meju's (1994) form of the **MRM** for Marquardt Inversion if you replace the $\beta\mathbf{I}$ in his Expression (9.4) with a $\lambda^{(i)}\mathbf{W}^T\mathbf{W}$ and don't include an apriori model).

Appendix B : Derivation of the Model Covariance Matrix

Here we expand on the work of Materese (1993) to derive a version of the posterior model covariance matrix for the inversion method employed here, and a Monte Carlo technique to determine it, that is similar to the Maximum Likelihood Method (MLM) of Tarantola(1987) and Tarantola and Vallete (1982). Linearizing about a given model, the MLM functional that they propose to minimize can be written as

$$S = \left[(\mathbf{d_m} - \mathbf{d}^{(i)} - \mathbf{A}^{(i)}(\mathbf{m}^{(i+1)} - \mathbf{m}^{(i)}))^T \mathbf{C_d}^{-1}(\mathbf{d_m} - \mathbf{d}^{(i)} - \mathbf{A}^{(i)}(\mathbf{m}^{(i+1)} - \mathbf{m}^{(i)}))\right] \qquad \text{(B1)}$$

$$+(\mathbf{m_{ref}} - \mathbf{m}^{(i+1)})^T \mathbf{C_m}^{-1}(\mathbf{m_{ref}} - \mathbf{m}^{(i+1)}).$$

Here $\mathbf{C_d}$ is the data covariance matrix which contains specifics about the estimated data errors, $\mathbf{C_m}$ is the apriori model covariance matrix which contains information about how parameters within the model domain are correlated to one another, and $\mathbf{m_{ref}}$ is a reference model. Often, $\mathbf{C_m}$ is precomputed to be equal to a constant variance times a spatially varying function of some sort (Tarantola and Vallette, 1982), i.e.,

$$\mathbf{C_m} = \sigma_m^2 \mathbf{F} \qquad \text{(B2)}$$

where σ_m^2 is an assumed constant model variance and $\mathbf{F}$ describes how different points within the model domain are correlated. Note, if the data error is uncorrelated, and because our data weighting matrices are the inverse of the data standard deviations, $\mathbf{C_d}^{-1} = \mathbf{D}^T\mathbf{D}$.

Now let us write the minimization functional for our inversion technique, which is given in Newman and Alumbaugh (1997, equation 1) as

$$S=\left[(\mathbf{d_m}-\mathbf{d}^{(i)}-\mathbf{A}^{(i)}(\mathbf{m}^{(i+1)}-\mathbf{m}^{(i)}))^T\mathbf{D}^T\mathbf{D}(\mathbf{d_m}-\mathbf{d}^{(i)}-\mathbf{A}^{(i)}(\mathbf{m}^{(i+1)}-\mathbf{m}^{(i)})\right]$$

$$+\lambda^{(i)}(\mathbf{Wm}^{(i+1)})^T(\mathbf{Wm}^{(i+1)}). \qquad \text{(B3)}$$

Notice that the difference between equations (B1) and (B3) is the last term. Matarese (1993) showed that the last term in this functional can be written such that

$$S=\left[(\mathbf{d_m}-\mathbf{d}^{(i)}-\mathbf{A}^{(i)}(\mathbf{m}^{(i+1)}-\mathbf{m}^{(i)}))^T\mathbf{D}^T\mathbf{D}(\mathbf{d_m}-\mathbf{d}^{(i)}-\mathbf{A}^{(i)}(\mathbf{m}^{(i+1)}-\mathbf{m}^{(i)}))\right]$$

$$+\lambda^{(i)}(0-\mathbf{Wm}_{i+1})^T(0-\mathbf{Wm}_{i+1}). \qquad \text{(B4)}$$

Making some simple substitutions, we can further rearrange equation (B4) as

$$S=\left[(\mathbf{d_m}-\mathbf{d}^{(i)}-\mathbf{A}^{(i)}(\mathbf{m}^{(i+1)}-\mathbf{m}^{(i)}))^T\mathbf{D}^T\mathbf{D}(\mathbf{d_m}-\mathbf{d}^{(i)}-\mathbf{A}^{(i)}(\mathbf{m}^{(i+1)}-\mathbf{m}^{(i)}))\right]$$

$$+\left[(\mathbf{n}-\mathbf{Wm}^{(i+1)})^T\lambda^{(i)}(\mathbf{n}-\mathbf{Wm}^{(i+1)})\right]. \qquad \text{(B5)}$$

where **n** is a zero vector. Comparing this to Equation (B1) shows that rather than forcing the inverted model to be close to a reference model, here we are attempting to force the curvature between adjacent model parameters to be close to zero.

Minimizing equation (B1) yields

$$\mathbf{m}^{(i+1)}=\left[\mathbf{A}^{(i)^T}\mathbf{C_d}^{-1}\mathbf{A}^{(i)}+\mathbf{C_m}^{-1}\right]^{-1}\left[\mathbf{A}^{(i)^T}\mathbf{C_d}^{-1}(\mathbf{d_m}-\mathbf{d}^{(i)}+\mathbf{A}^{(i)}\mathbf{m}^{(i)})+\mathbf{C_m}^{-1}\mathbf{m_{ref}}\right] \qquad \text{(B6)}$$

which is equivalent to Tarantola and Valette's (1982) equation 25. Similarly if we minimize equation (B5) we arrive at

$$\mathbf{m}^{(i+1)}=\left[\mathbf{A}^{(i)^T}\mathbf{D}^T\mathbf{D}\mathbf{A}^{(i)}+\lambda^{(i)}\mathbf{W}^T\mathbf{W}\right]^{-1}\cdot$$

$$\left[\mathbf{A}^{(i)^T}\mathbf{D}^T\mathbf{D}(\mathbf{d_m}-\mathbf{d}^{(i)}+\mathbf{A}^{(i)}\mathbf{m}^{(i)})+\lambda^{(i)}\mathbf{W}^T\mathbf{n}\right]. \qquad \text{(B7)}$$

Tarantola (1987) gives an estimate of the posterior model covariance matrix for equation (B6) to be

$$\mathbf{MCM}_{mlm} = \left[\mathbf{A}^{(i)T}\mathbf{C}_\mathbf{d}^{-1}\mathbf{A}^{(i)} + \mathbf{C}_\mathbf{m}^{-1}\right]^{-1}. \tag{B8}$$

If we take the same term from equation 7, the **MCM** for our inversion scheme is given as

$$\mathbf{MCM}_{NA} = \left[\mathbf{A}^{(i)T}\mathbf{D}^T\mathbf{D}\mathbf{A}^{(i)} + \lambda^{(i)}\mathbf{W}^T\mathbf{W}\right]^{-1} \tag{B9}$$

which agrees with similar formulations for the inverse problem given in Meju (1994).

Tarantola(1987) also derives a Monte Carlo method for estimating the full nonlinear posterior model covariance matrix. This involves adding random data and reference model vectors to equation (B6),

$$\mathbf{m}^{(i+1)} = \left[\mathbf{A}^{(i)T}\mathbf{C}_\mathbf{d}^{-1}\mathbf{A}^{(i)} + \mathbf{C}_\mathbf{m}^{-1}\right]^{-1} \cdot \left[\mathbf{A}^{(i)T}\mathbf{C}_\mathbf{d}^{-1}(\mathbf{d}_\mathbf{m} - \mathbf{d}^{(i)} + \boldsymbol{\varepsilon}_l + \mathbf{A}^{(i)}\mathbf{m}^{(i)}) + \mathbf{C}_\mathbf{m}^{-1}(\mathbf{m}_\mathbf{ref} + \mathbf{h}_l)\right] \tag{B10}$$

and rerunning the full non linear inversion L times. Here $\boldsymbol{\varepsilon}_l$ is a random number vector of a variance equal to that of the estimated data noise, and $\mathbf{h}_l$ is a similar vector with a variance equal to σ_m^2. The mean of the resulting L model vectors yields the final model, and the non-linear **MCM** can be calculated using equation (13).

Matarese linearized this process about the final model for his inversion technique which yields a similar expression for our inversion method;

$$\mathbf{m}^{(i+1)} = \left[\mathbf{A}^{(i)T}\mathbf{D}^T\mathbf{D}\mathbf{A}^{(i)} + \lambda^{(i)}\mathbf{W}^T\mathbf{W}\right]^{-1} \cdot$$

$$\left[\mathbf{A}^{(i)T}\mathbf{D}^T\mathbf{D}(\mathbf{d_m} - \mathbf{d}^{(i)} + \boldsymbol{\varepsilon}_l + \mathbf{A}^{(i)}\mathbf{m}^{(i)}) + \lambda^{(i)}\mathbf{W}^T(\mathbf{n} + \mathbf{h}_l)\right] \quad \text{(B11)}$$

In doing so we are not only assuming that the data have errors present in them, but also that our assumption that the curvature between adjacent model parameters being zero is also in error, and the variance of that error is $1/\lambda$. Note, dropping the zero vector, $\mathbf{n}$, from this expression, and accounting for the logarithmic parameterization yields a form that is consistant with that given in Equation (12).

Figure Captions

Figure 1 - (a) Two dimensional cross well EM test model used for demonstrating the image appraisal techniques. The **X**'s in the left well represent vertical magnetic dipole source positions, and the **O**'s in the right well positions where measurements of the vertical magnetic field are made. The frequency of operation is 1KHz. (b) Non-linear inversion results (see the text for a description of the inversion parameters).

Figure 2 - The Resolution Radius calculated from the model resolution matrix for the image shown in Figure 1b.

Figure 3 - The point spread functions at four different points within the imaging domain as determined from the model resolution matrix for the image given in Figure 1b.

Figure 4 - The (a) horizontal 50% spread width and (b) vertical 50% spread width throughout the imaging domain given in Figure 1b as calculated from the model resolution matrix.

Figure 5 - Parameter uncertainty for the image given in Figure 1b that has been estimated via the main diagonal of the model covariance matrix. (a) Estimated parameter standard deviations. (b) Estimated parameter standard deviations normalized by the image in Figure 1b.

Figure 6 - Three dimensional model and image of the Richmond Field Station simulation given in Alumbaugh and Newman (1997). The results are shown in a series of depth slices ranging in depth from 10m to 50 m depth. The five dots on the uppermost depth slice represents the horizontal location of the five wells within the model, with the red representing the center transmitter well, and the four blue dots representing the receiver wells. Note, the color scale is logarithmic with red representing 1 S/m, and purple representing 0.004S/m. (a) Model. (b) Image.

Figure 7 - A three dimensional rendering of the point spread function for the point x=-3m, y=-3m, z=29m within the image domain depicted in Figure 6. (a) Isosurfaces describing the PSF values equal to ± 33% of the maximum value. Green is + 30%, blue is -30%. (b) Isosurface describing the PSF values equal to +67% of the maximum value.

Figure 8 - (a) A conductivity depth slice at Z=29m for the image in Figure 6. The white dots represent the well locations. (b) The 50% spread width in the X direction, (c) the Y direction, and (d) the Z direction. The black dots represent the points at which the PSF was determined. Interpolation between the dots was accomplished via Kriging.

Figure 9 - The main diagonal of the model covariance matrix for the image in Figure 1b as determined via the iterative method of Matarese (1993). The results should be compared to the analytic results given in Figure 5b. (a) L=25. (b)L=400.

Figure 10 - The square root of the main diagonal of the model covariance matrix for the image in Figure 6 normalized by the parameter values. Red represents a standard deviation of 4% of the parameter value, and blue 0.5%. (a) Depth slices of the standard deviation presented in the same format as the image in Figure 6. (b) Volume rendering of the standard deviation with all values greater than 2% of the parameter value made invisible.

Figure 11 - Imaging results of the data set collected at the Lost Hills Oil Field in the Central Valley of California. The image has been plotted with the induction logs collected in each of the wells. **X's** represent VMD source positions, and the **O**'s the receiver points where measurements of the vertical magnetic field were made. The frequency of operation was approximately 1KHz. The black lines across the image plane are simply connecting the upper and lower most transmitters and receivers to better define the optimal imaging region.

Figure 12 - The 50% spread widths in the (a) horizontal and (b) vertical direction for the image in Figure 11.

Figure 13 - The square root of the main diagonal of the model covariance matrix for the image in Figure 11. (a) Estimated parameter standard deviations, and (b) estimated parameter standard deviations normalized by the parameter values in Figure 11.

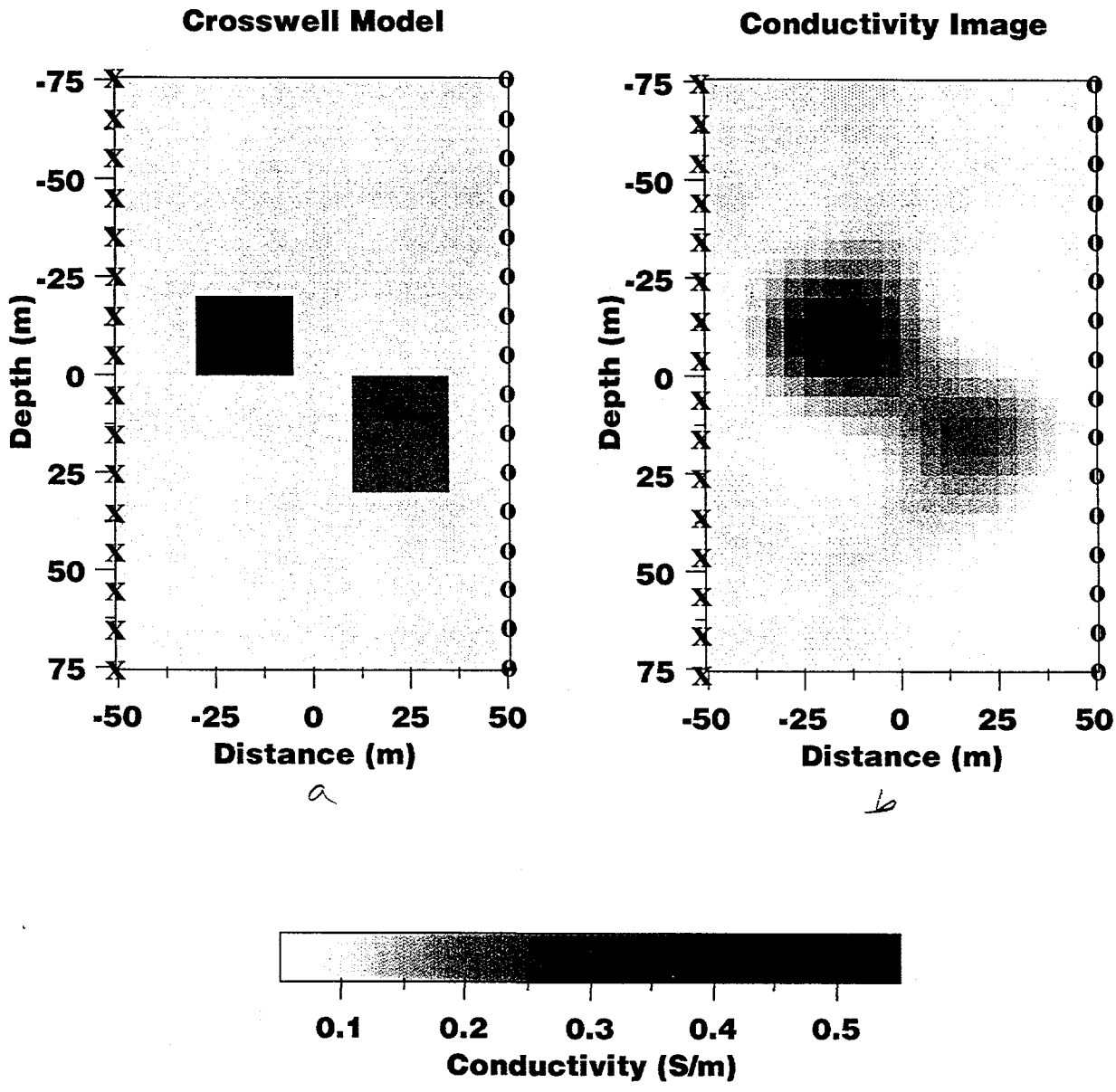
Crosswell Model
Conductivity Image
-75
-50
-25
0
25
50
75
Depth (m)
-50
-25
0
25
50
Distance (m)
a
b
0.1
0.2
0.3
0.4
0.5
Conductivity (S/m)

Fig 1

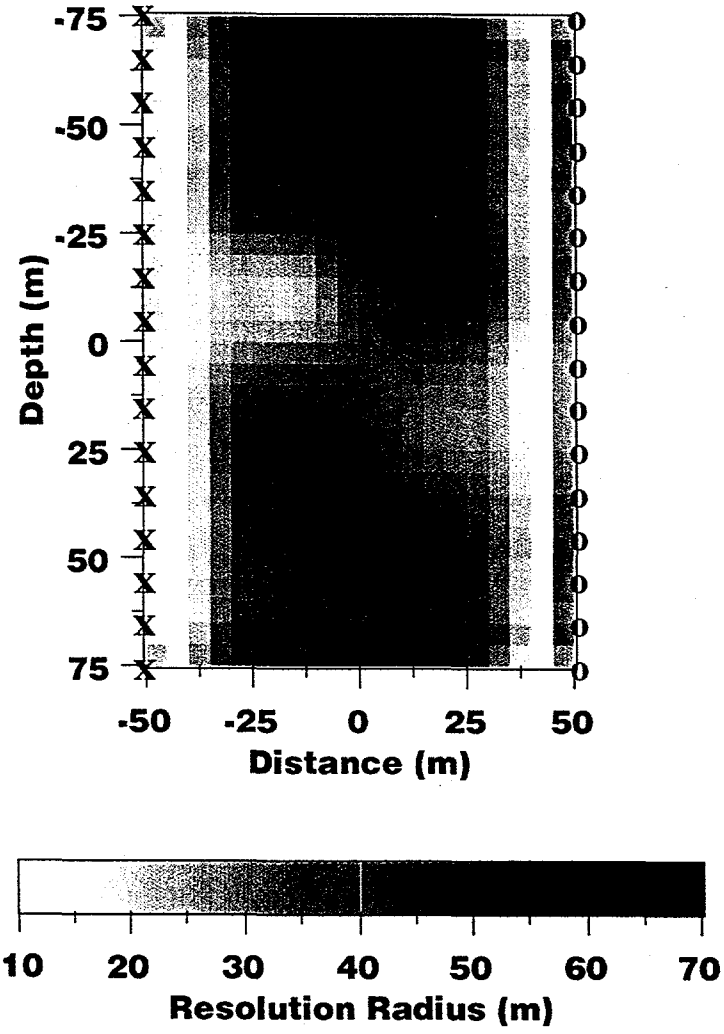
-75
-50
-25
0
25
50
75
Depth (m)
-50
-25
0
25
50
Distance (m)
10
20
30
40
50
60
70
Resolution Radius (m)

Fig 2

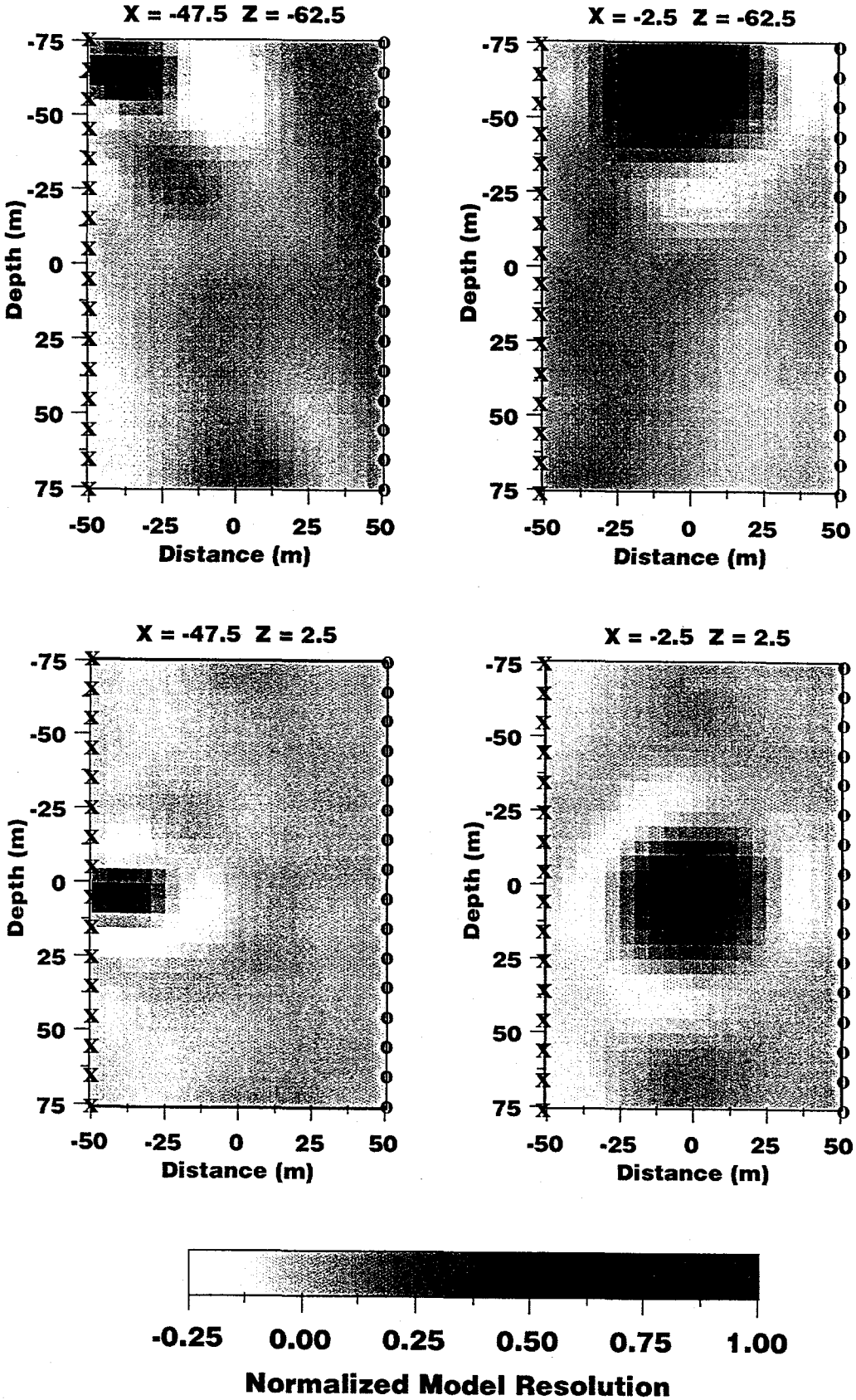
X = -47.5 Z = -62.5
X = -2.5 Z = -62.5
X = -47.5 Z = 2.5
X = -2.5 Z = 2.5
Depth (m)
Distance (m)
-75
-50
-25
0
25
50
75
-0.25
0.00
0.25
0.50
0.75
1.00
Normalized Model Resolution

Fig 3

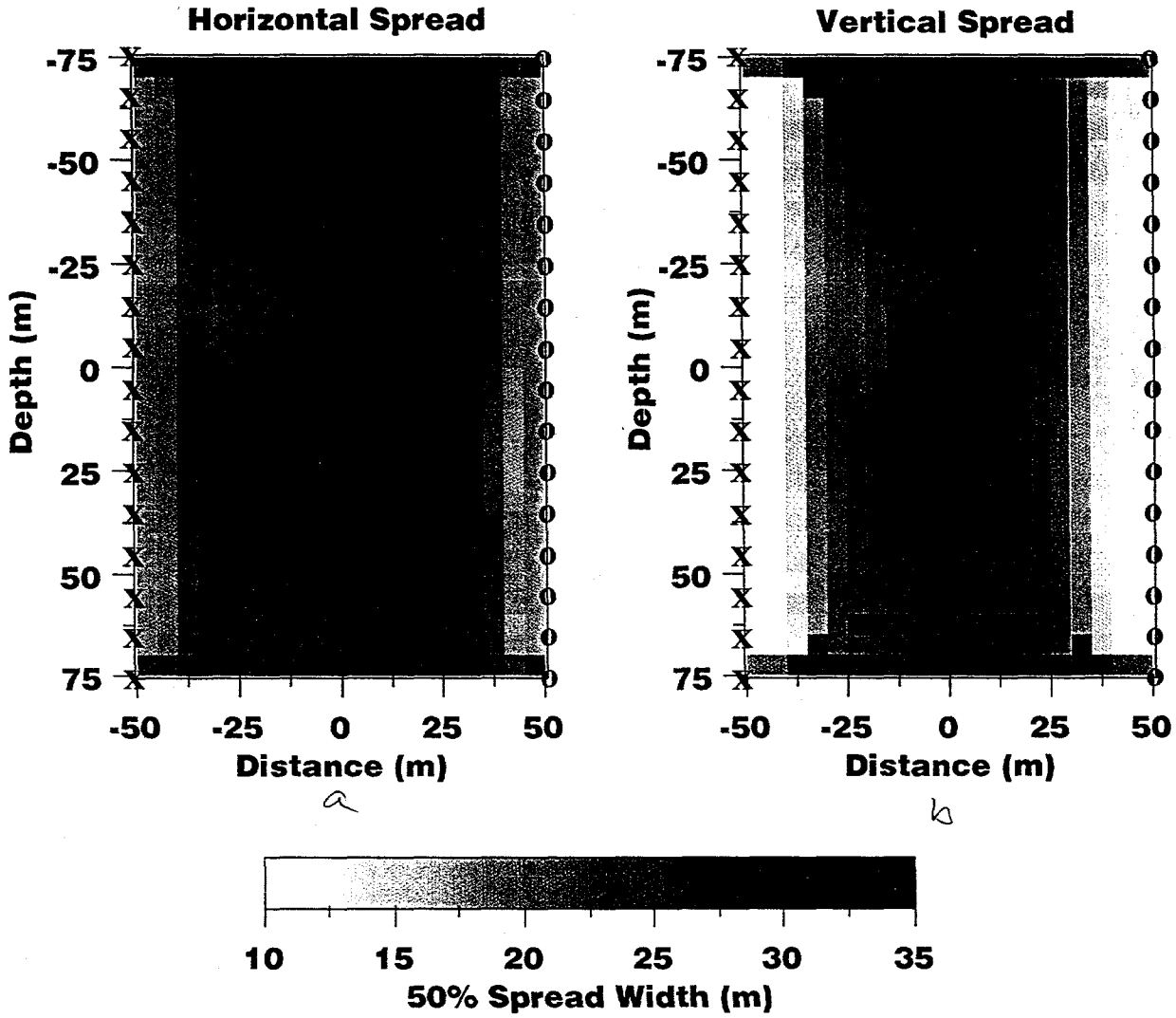
Horizontal Spread
Vertical Spread
Depth (m)
-75
-50
-25
0
25
50
75
-50
-25
0
25
50
Distance (m)
a
b
10
15
20
25
30
35
50% Spread Width (m)

Fig 4

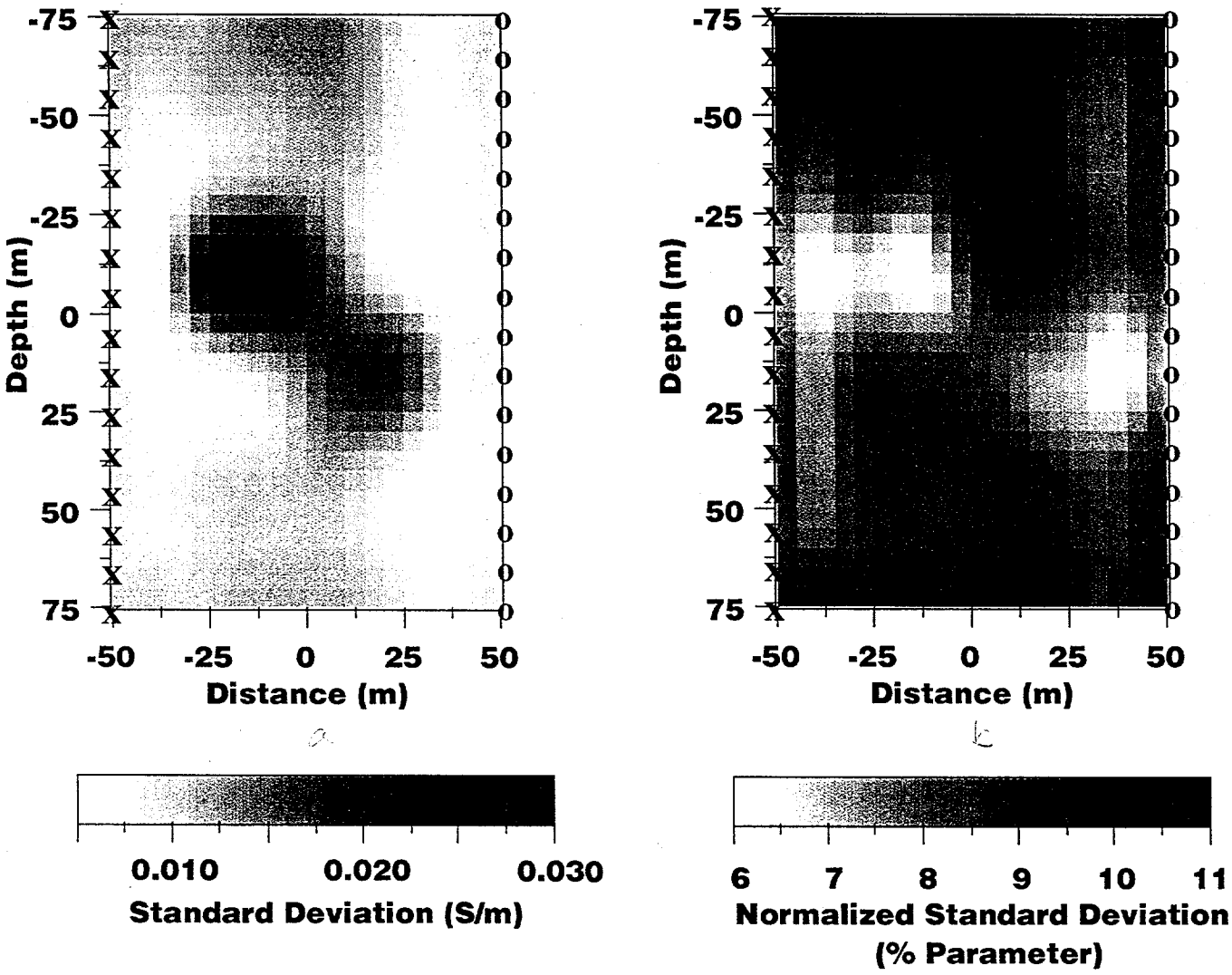
-75
-50
-25
0
25
50
75
Depth (m)
-50
-25
0
25
50
Distance (m)
a
0.010
0.020
0.030
Standard Deviation (S/m)
b
6
7
8
9
10
11
Normalized Standard Deviation
(% Parameter)

Fig 5

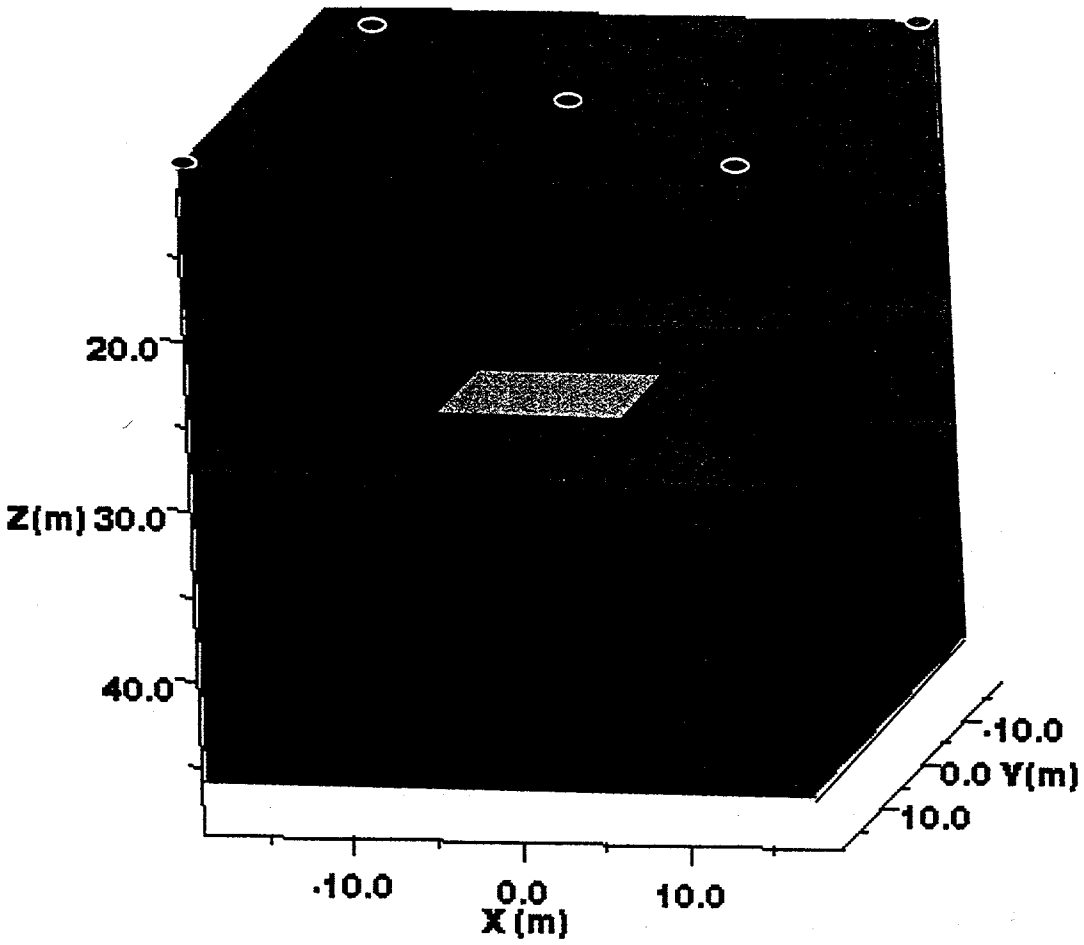

9

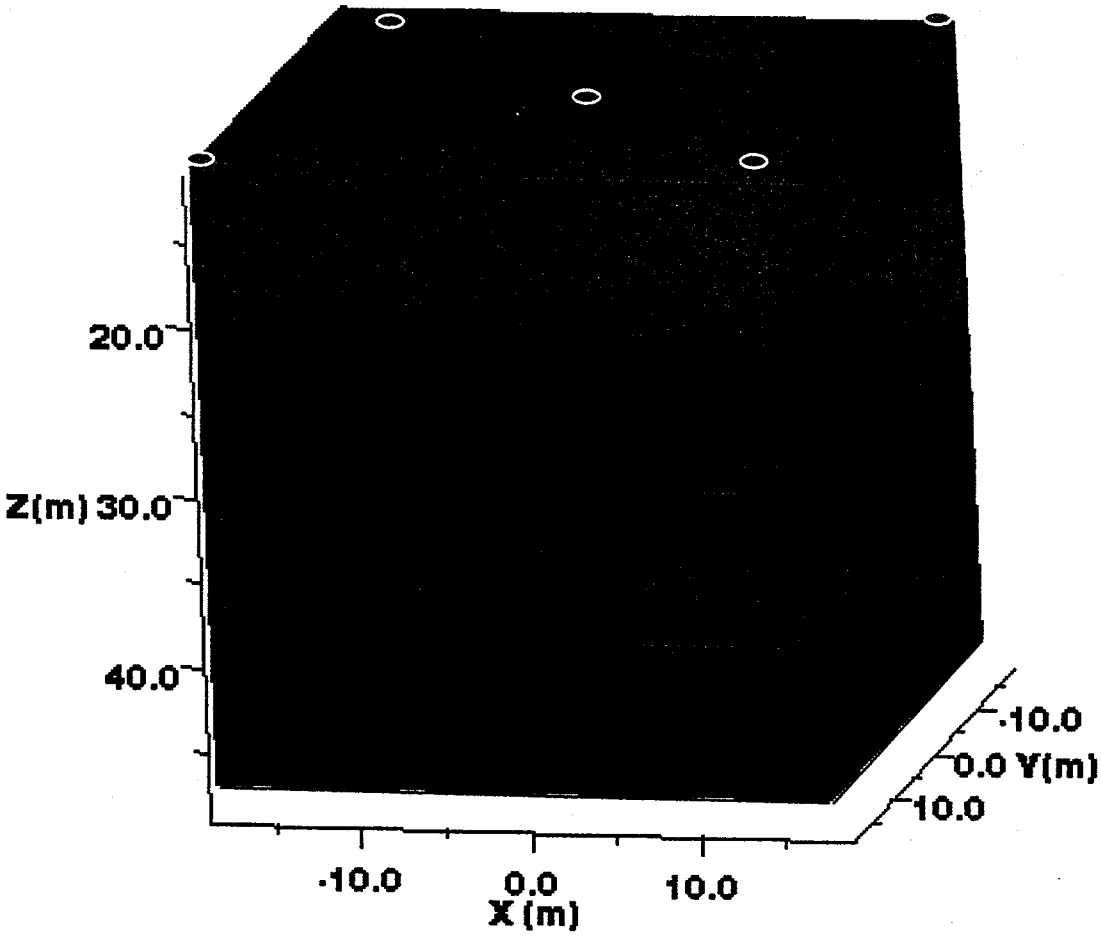

6

Fig 6

Color scale?

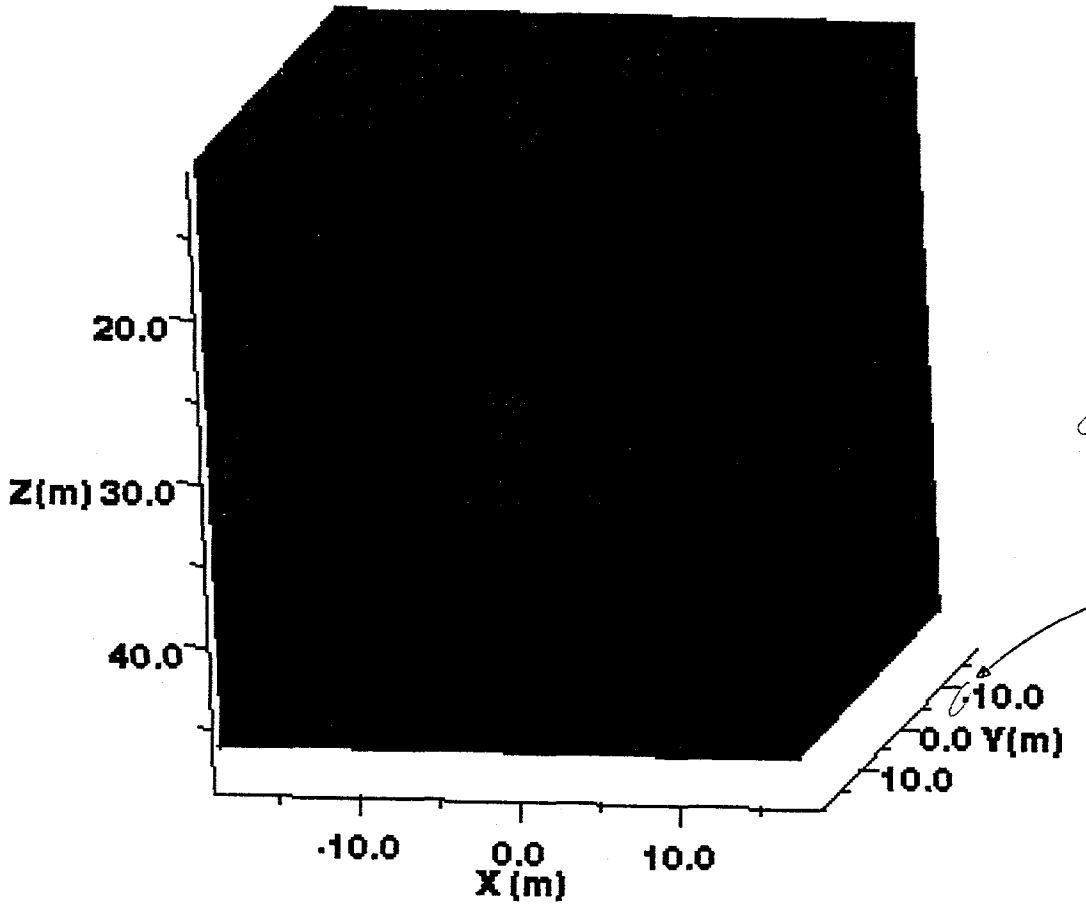
20.0
Z(m) 30.0
40.0
10.0
0.0 Y(m)
10.0
-10.0
0.0
10.0
X (m)

a

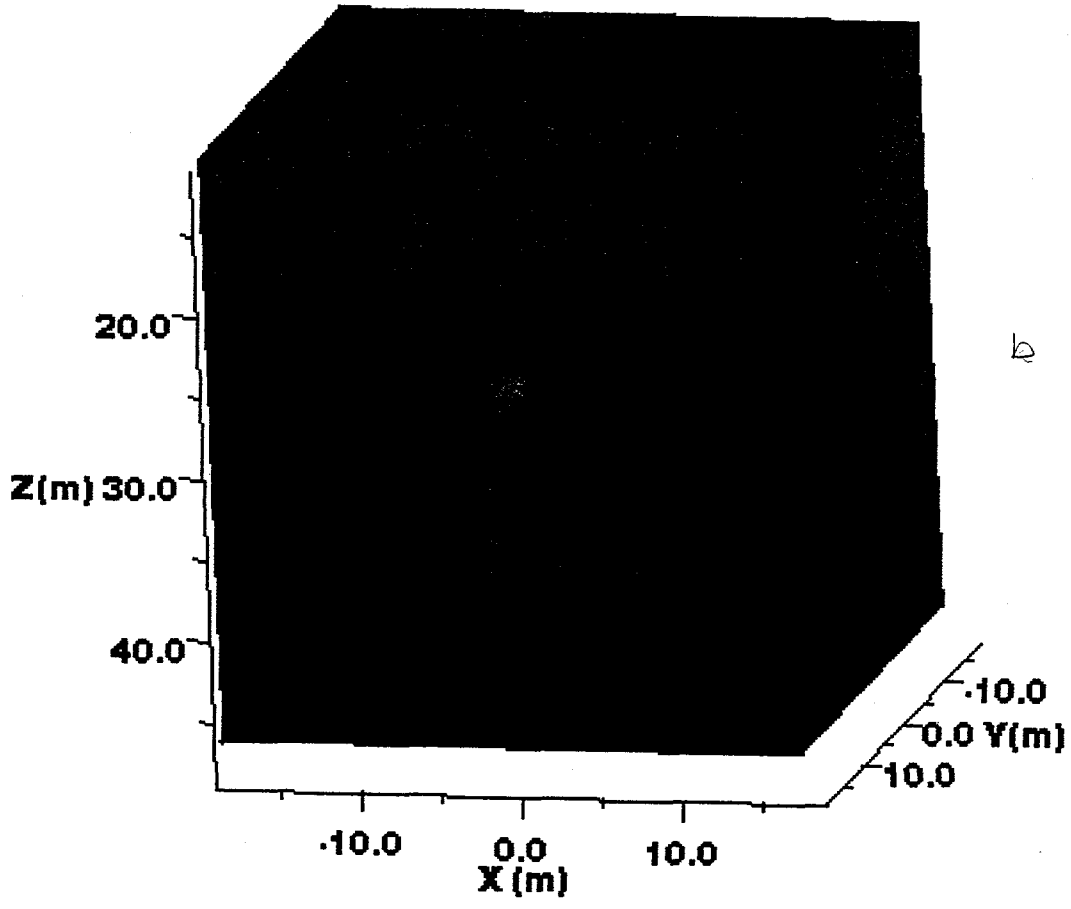
20.0
Z(m) 30.0
40.0
-10.0
0.0 Y(m)
10.0
-10.0
0.0
10.0
X (m)

b

Fig 7

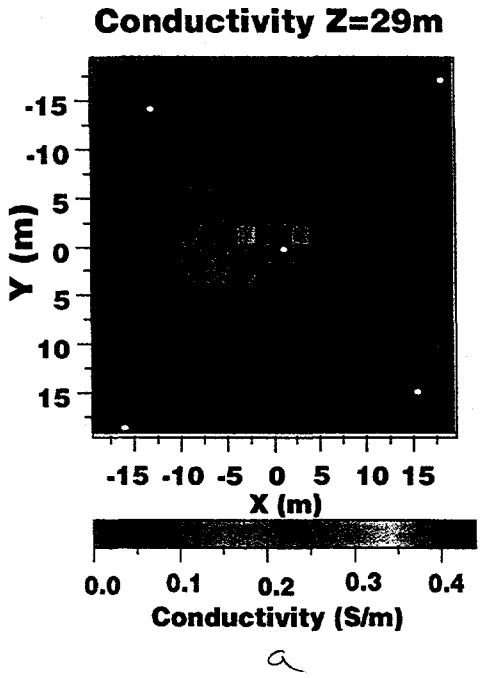
Conductivity Z=29m
Y (m)
-15
-10
5
0
5
10
15
-15 -10 -5 0 5 10 15
X (m)
0.0 0.1 0.2 0.3 0.4
Conductivity (S/m)

a

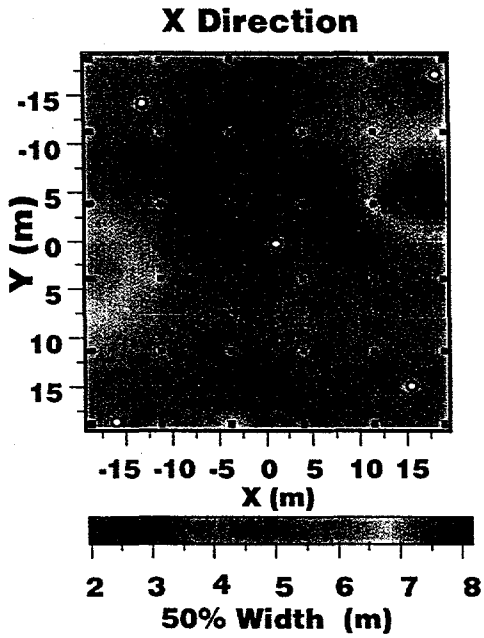
X Direction
Y (m)
-15
-10
5
0
5
10
15
-15 -10 -5 0 5 10 15
X (m)
2 3 4 5 6 7 8
50% Width (m)

b

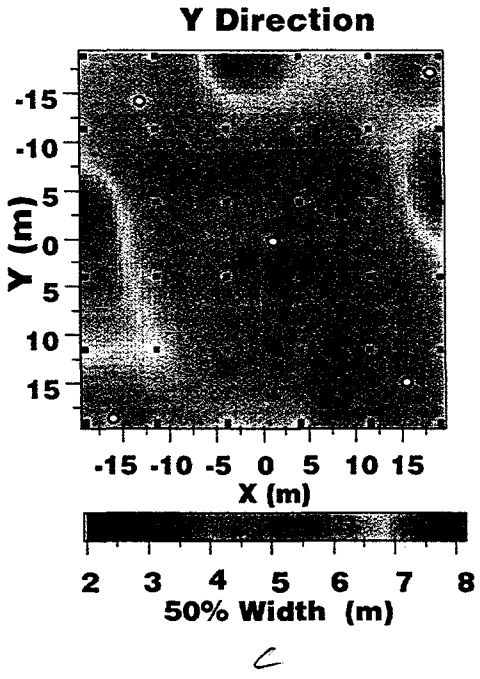
Y Direction
Y (m)
-15
-10
5
0
5
10
15
-15 -10 -5 0 5 10 15
X (m)
2 3 4 5 6 7 8
50% Width (m)

c

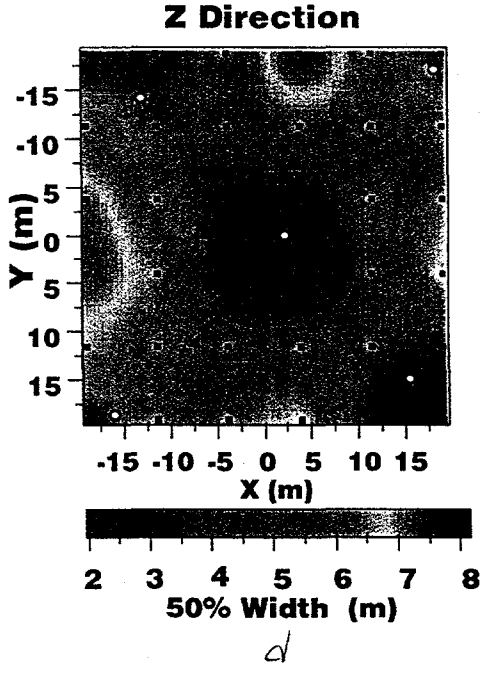
Z Direction
Y (m)
-15
-10
5
0
5
10
15
-15 -10 -5 0 5 10 15
X (m)
2 3 4 5 6 7 8
50% Width (m)

d

Fig 8

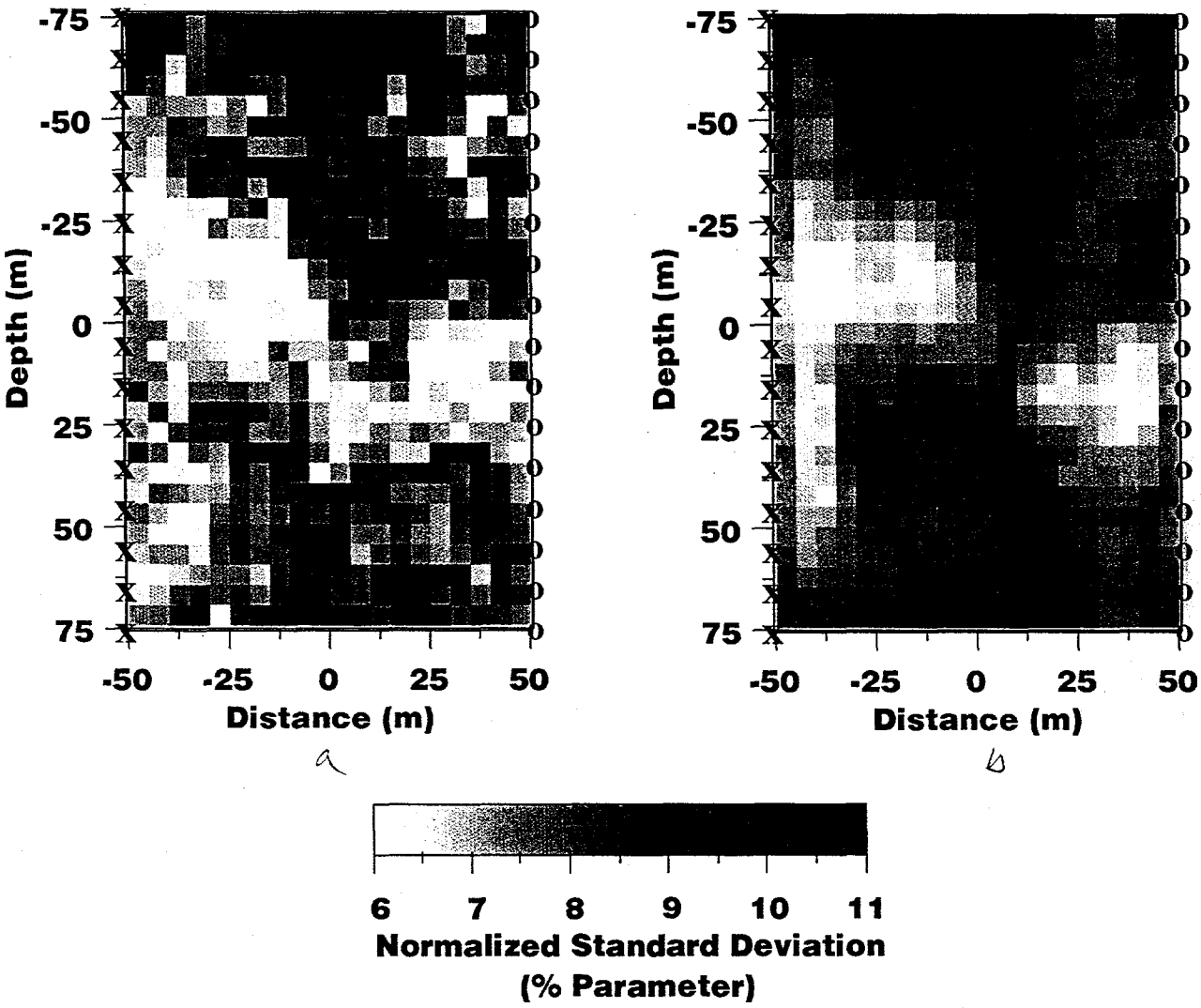
-75
-50
-25
0
25
50
75
Depth (m)
-50
-25
0
25
50
Distance (m)
a
-75
-50
-25
0
25
50
75
Depth (m)
-50
-25
0
25
50
Distance (m)
b
6
7
8
9
10
11
Normalized Standard Deviation
(% Parameter)

Fig 9

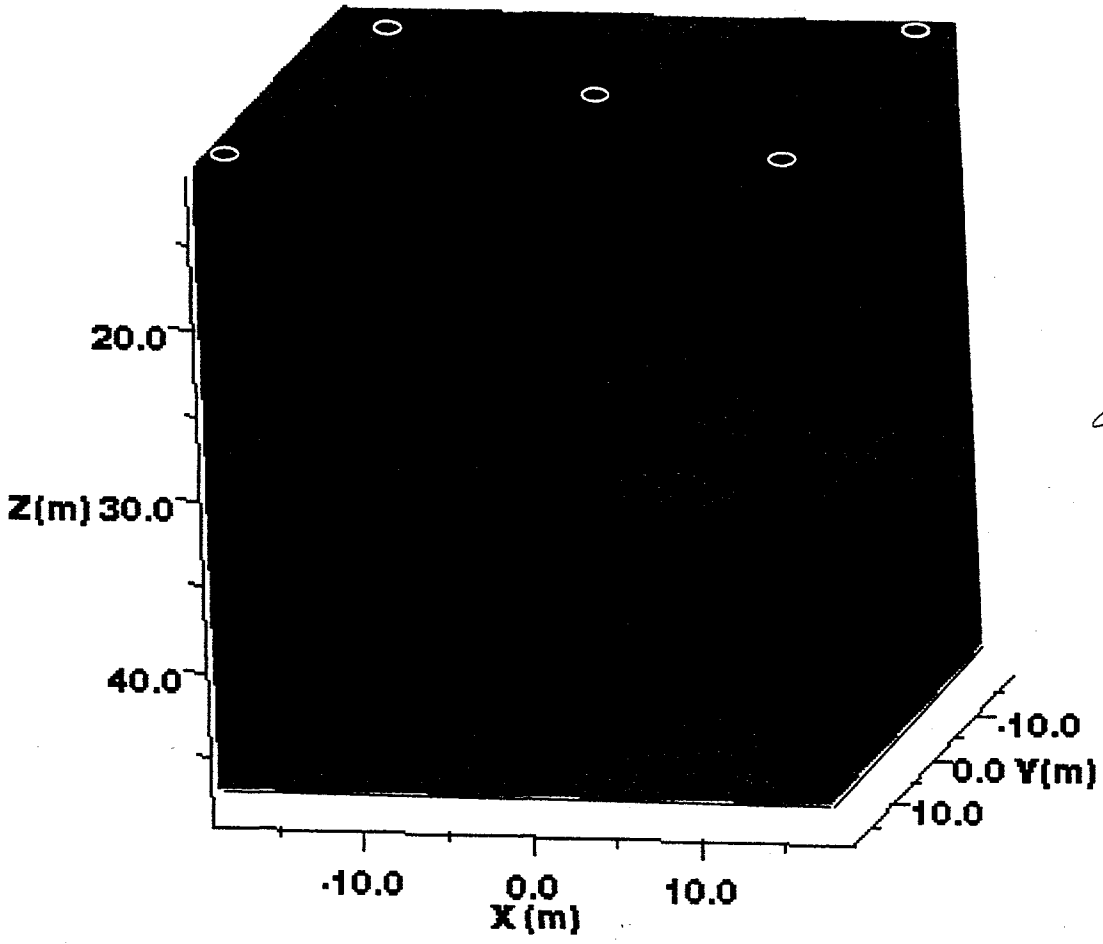
20.0
Z(m) 30.0
40.0
-10.0
0.0 Y(m)
10.0
-10.0
0.0
10.0
X (m)

a

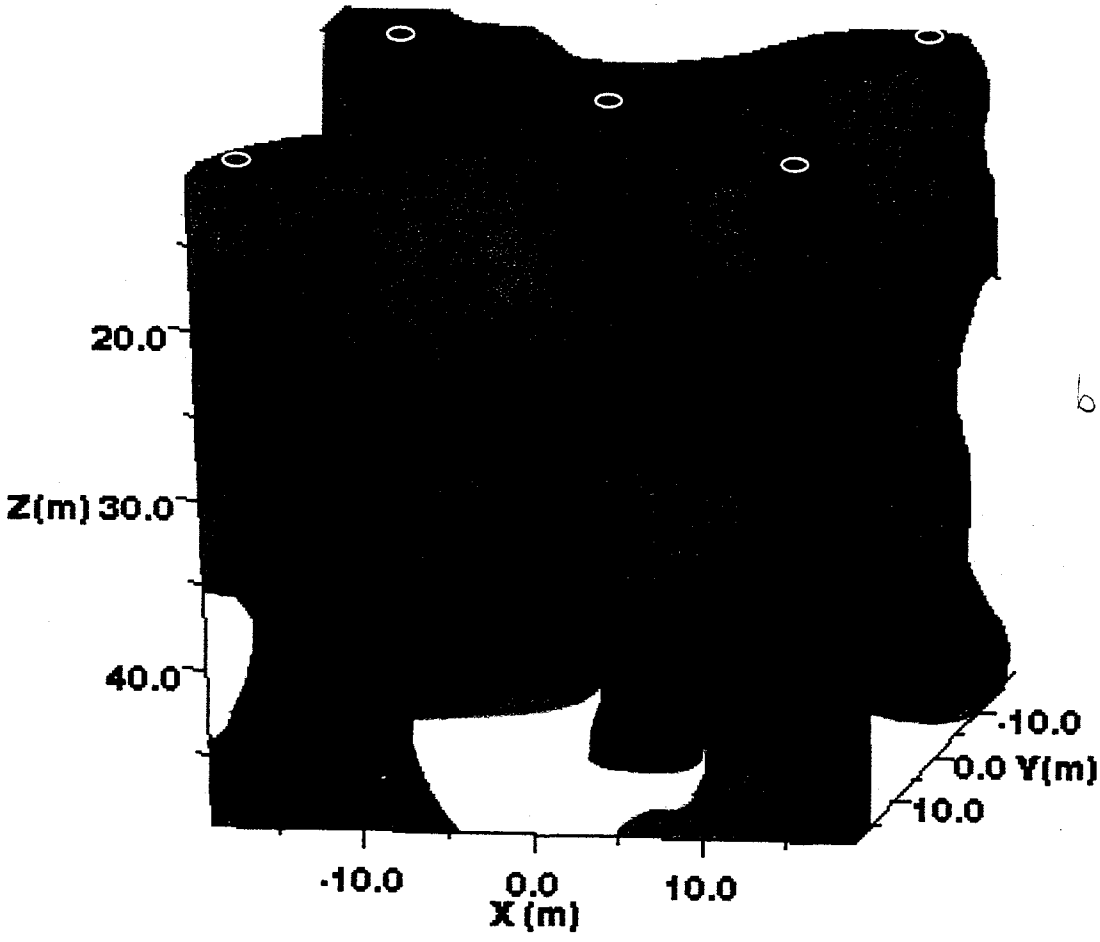
20.0
Z(m) 30.0
40.0
-10.0
0.0 Y(m)
10.0
-10.0
0.0
10.0
X (m)

b

Fig 10

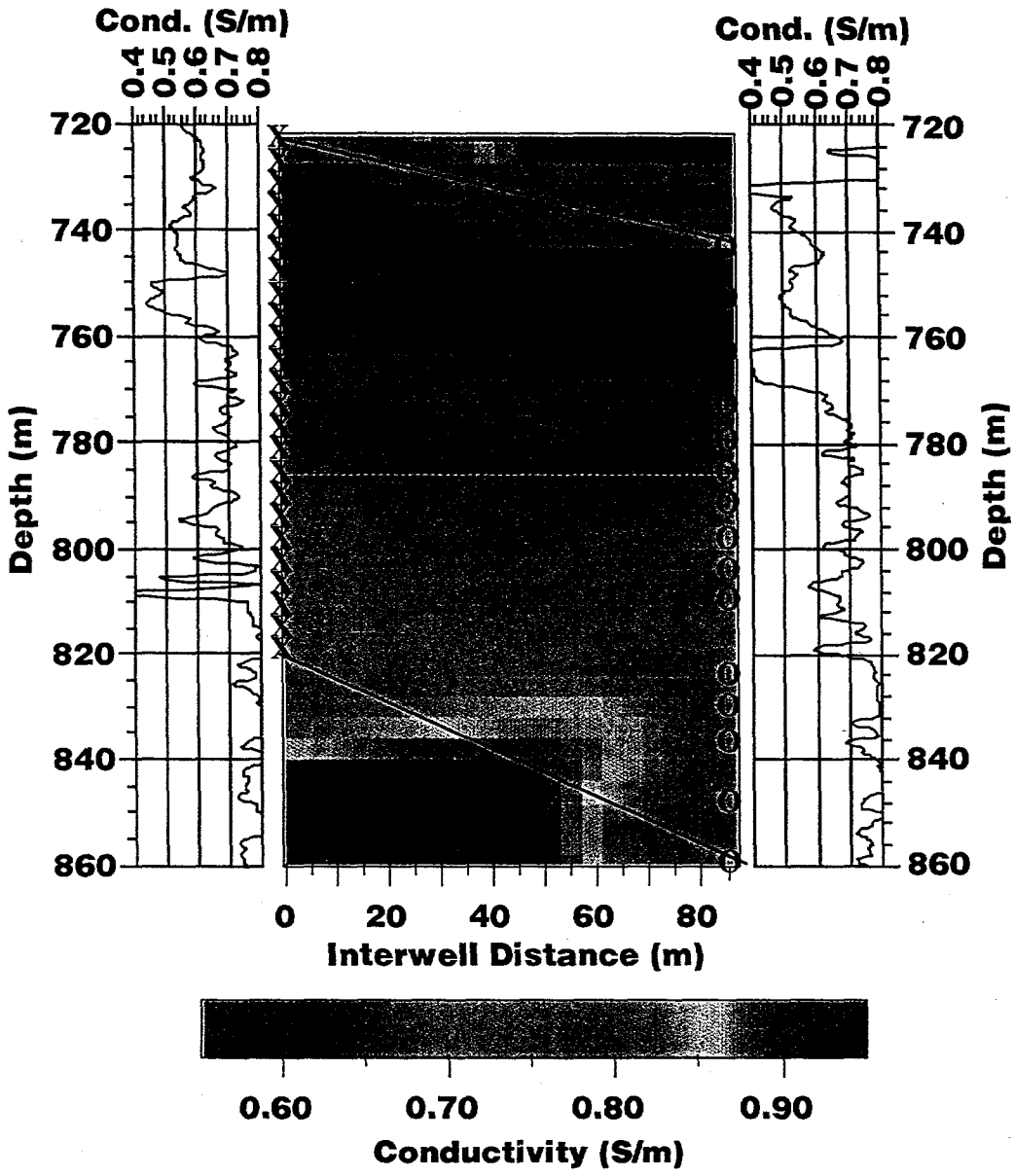
Cond. (S/m)
0.4
0.5
0.6
0.7
0.8
Cond. (S/m)
0.4
0.5
0.6
0.7
0.8
720
740
760
780
800
820
840
860
Depth (m)
Depth (m)
0
20
40
60
80
Interwell Distance (m)
0.60
0.70
0.80
0.90
Conductivity (S/m)

Fig 1

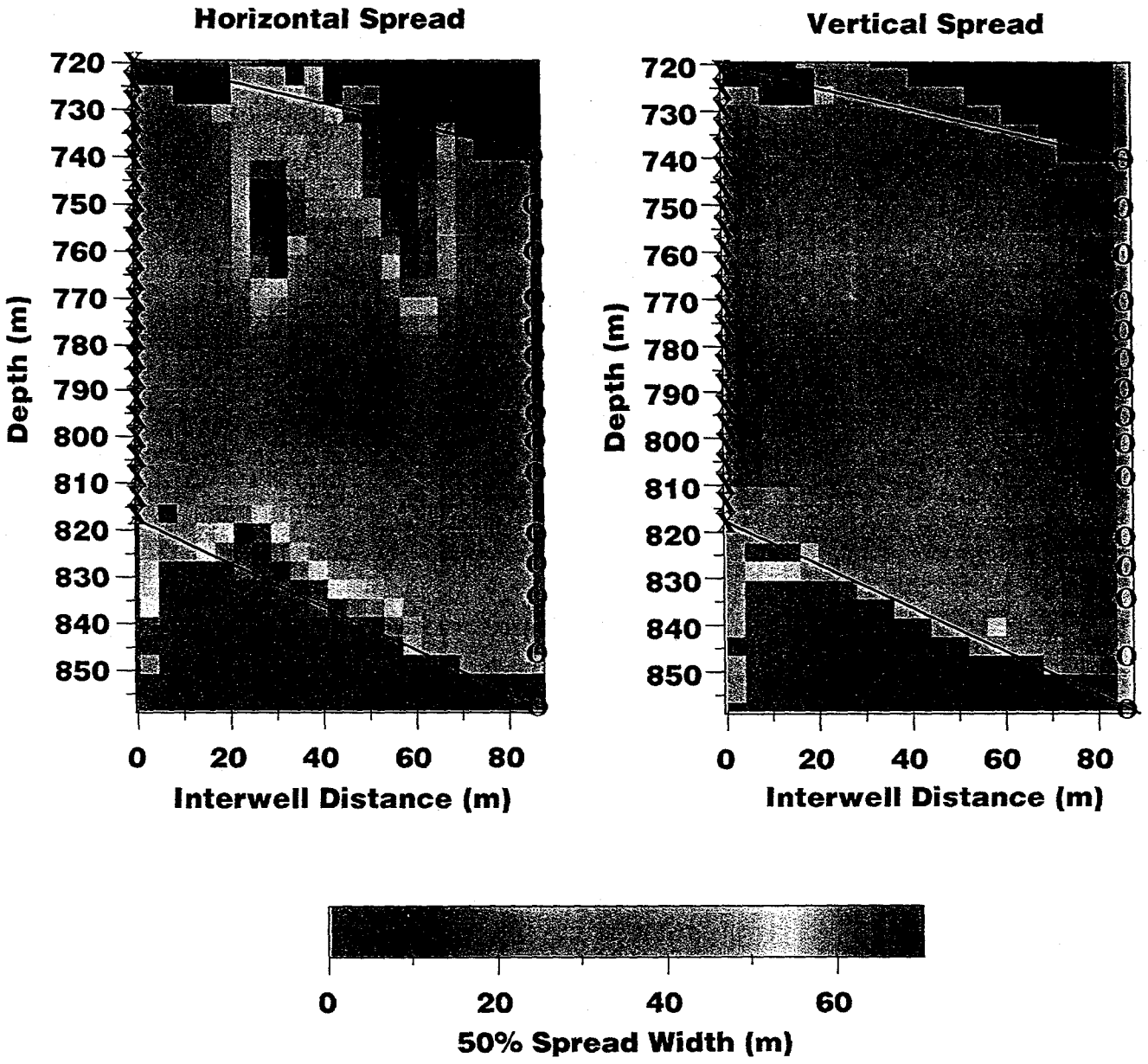
Horizontal Spread
Vertical Spread
Depth (m)
720
730
740
750
760
770
780
790
800
810
820
830
840
850
0
20
40
60
80
Interwell Distance (m)
0
20
40
60
50% Spread Width (m)

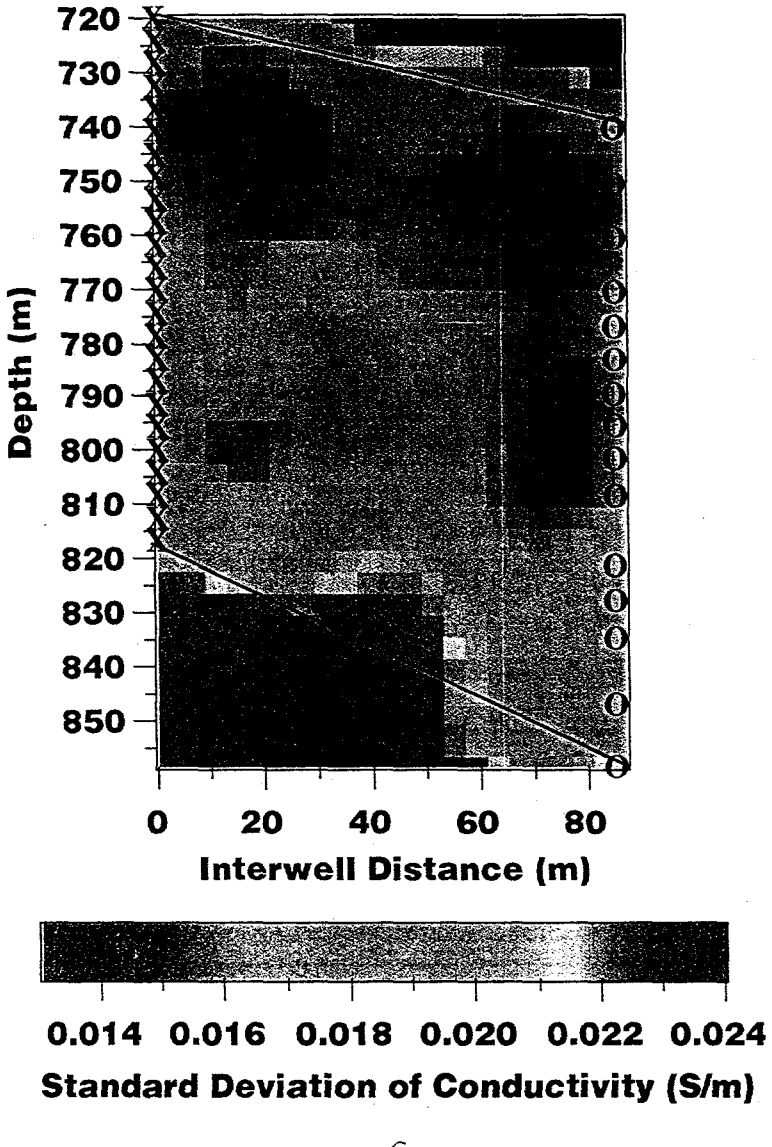
720
730
740
750
760
770
780
790
800
810
820
830
840
850
Depth (m)
0
20
40
60
80
Interwell Distance (m)

0.014
0.016
0.018
0.020
0.022
0.024
Standard Deviation of Conductivity (S/m)

a

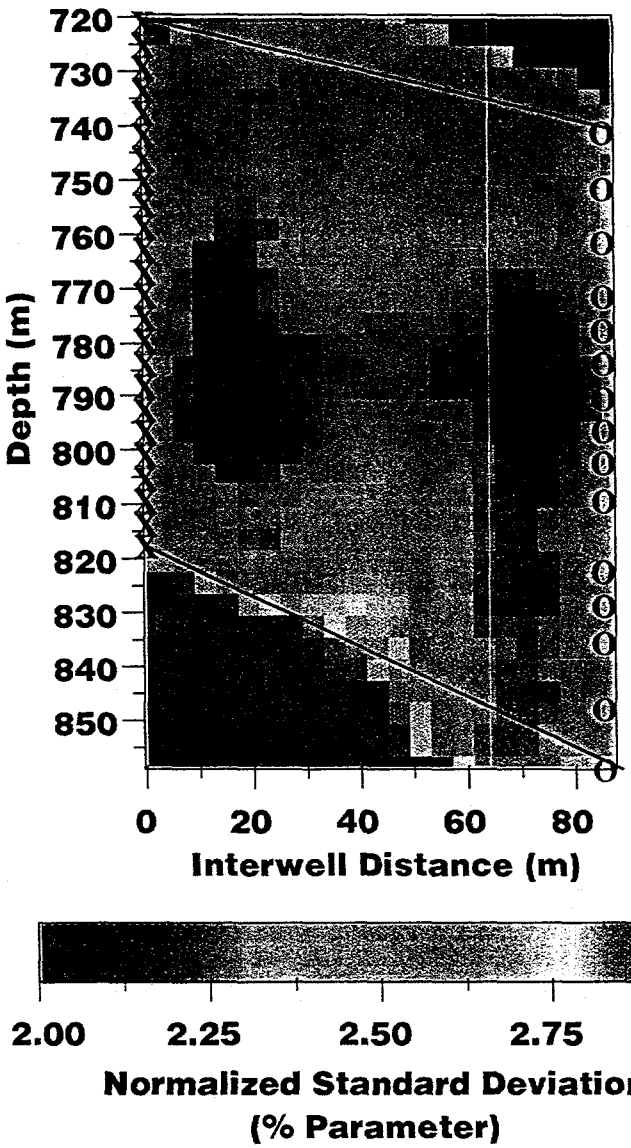
720
730
740
750
760
770
780
790
800
810
820
830
840
850
Depth (m)
0
20
40
60
80
Interwell Distance (m)

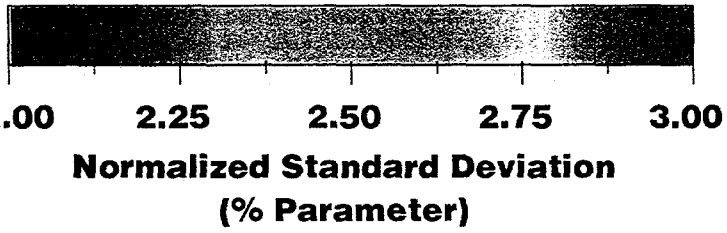
2.00
2.25
2.50
2.75
3.00
Normalized Standard Deviation
(% Parameter)

b

Fig 13